Unravelling the effect of Ti^{3+}/Ti^{4+} active sites dynamic on reaction pathways in direct gas-solid-phase CO_2 photoreduction

Niket S. Powar [a], Sanghoon Kim [b], Junho Lee [a], Eunhee Gong [a], Chaitanya B. Hiragond [a], Dongyun Kim [a], Tierui Zhang [c,d], Minho Kim [b,*], Su-Il In [a,e,**]

[a] *Department of Energy Science & Engineering, Daegu Gyeongbuk Institute of Science and Technology (DGIST), Daegu 42988, Republic of Korea*
[b] *Department of Applied Chemistry, Kyung Hee University, Yongin, Gyeonggi 17104, Republic of Korea*
[c] *Key Laboratory of Photochemical Conversion and Optoelectronic Materials, Technical Institute of Physics and Chemistry, Chinese Academy of Sciences, Beijing 100190, China*
[d] *Center of Materials Science and Optoelectronics Engineering, University of Chinese Academy of Sciences, Beijing 100049, China*
[e] *Materials and Process Simulation Center, California Institute of Technology, Pasadena, CA 91125, United States*

ARTICLE INFO

ABSTRACT

Converting CO_2 to CH_4 by solar-powered catalysis involves complex steps that produce a range of by-products. Therefore, designing efficient heterostructures for a particular chemical synthesis is challenging. The optimisation of photocatalyst surfaces can achieve the desired CO_2 photoreduction pathway. Herein, we developed TiO_2/CdSe nanocrystals with both amorphous and crystalline TiO_2 surfaces. *In situ* EXAFS analysis revealed that the amorphous surface contains abundant active Ti^{3+} sites, while the crystalline surface is limited. Moreover, the amorphous surface of TiO_2/CdSe exhibits self-regenerating Ti^{3+} active sites, which enable a novel CH_4 cycle. Density functional theory calculation showed that an amorphous structure enhances electron transfer and localisation to Ti^{3+}, favouring CO_2 adsorption. *In situ* DRIFTS analysis showed different CO_2 to CH_4 pathways on both surfaces. These results show the potential for enhanced photocatalytic CO_2 reduction through surface engineering, which has far-reaching implications for sustainable energy conversion.

1. Introduction

Artificial photosynthesis to harness light and reduce CO_2 is vital in producing sustainable fuels and eco-friendly chemicals [1,2]. In order to accomplish efficient catalytic redox processes, it is essential to develop a unified catalyst system that combines a light absorber with a catalyst reaction. Heterostructures present a viable solution to achieve this objective [3–5]. Heterostructures can widen the light absorption spectrum and prevent the recombination of charge carriers. Consequently, the development of heterostructures has seen substantial progress over the past few decades [6–9]. To generate C_1 products, the photocatalyst must facilitate multiple proton-coupled electron transfer processes [10–12]. Transferring charges at the interface also plays a pivotal role in heterostructures, necessitating minimal resistance to enable optimal charge transport to CO_2 molecules [13]. Several research endeavours have been undertaken to advance heterostructures for CO_2

photoreduction [14–16]. Despite significant endeavours, achieving the desired efficiency of photoconversion of CO_2 into hydrocarbon fuel is an ongoing challenge. A comprehensive examination of prior studies suggests that utilising amorphous catalysts could effectively convert CO_2 to hydrocarbon products [17,18]. Wei *et al.* introduced the concept of an amorphous–crystalline heterostructure, exemplified by CeO_2@-CeO_2/A–TiO_2 [19]. They engineered a multi-shell structure for A–TiO_2, which developed novel insights, including a two-step reaction pathway wherein CO is initially generated and converted to CH_4. This heterostructure of A–TiO_2 provides active sites and enhances the local concentration of CO generation, further enabling the reduction of these CO molecules into CH_4. Wang *et al.* explored a CdSe quantum-dot-sensitised TiO_2 heterostructure for the gas-phase CO_2 photocatalytic reduction [20]. Their study revealed that CH_4 serves as the primary product of the reaction, accompanied by secondary products like CH_3OH, H_2, and CO. Introducing Pt as a cocatalyst into this heterostructure led to

---

performance improvements. The optimal yields for CH_4 and CH_3OH reached 48 and 3.3 ppm g^{-1} h^{-1} under visible light conditions, respectively. The study also suggested that the efficiency of CdSe-sensitized Pt/TiO_2 heterostructured catalysts could be further enhanced by optimising parameters, such as the concentrations of CdSe quantum dots and Pt cocatalysts, as well as by controlling the structure of CdSe/TiO_2 through various growth methods. The product's selectivity depends on several factors, including photon energy, conduction band position, light harvesting intensity, active surface sites, and the adsorption and desorption of reaction intermediates. The interaction between CO_2 molecules and the active surface sites is crucial in determining the reaction pathways, which is a significant challenge to control [21].

Amorphous catalysts containing numerous internal and external catalytic sites enable complex materials to undergo multi-step conversion reactions. Additionally, the presence of oxygen vacancies and Ti^{3+}/Ti^{4+} combinations in A—TiO_2 produces lattice electrons that reduce the lowest unoccupied molecular orbital (LUMO) energy of the CO_2 molecule [22–26]. Li et al. investigated C-TiO_2@A-TiO_{2-x}(OH)$_y$, where Ti^{3+} plays a crucial role in enhancing the photocatalytic reduction of CO_2 to CO. The amorphous shell was shown to possess surface-frustrated Lewis pairs (SFLPs) involving Ti^{3+}. These SFLPs are formed by quasi-dative bonds between the Lewis base's hydroxyl groups (OH) at the surface and the mixed valence Ti^{3+}/Ti^{4+}. This interaction is represented as HO-Ti^{3+}-[O]-Ti^{4+}. The Ti^{3+} species located within the disordered surface are essential for the formation and reactivity of these SFLPs. In particular, the Ti^{3+} species within the SFLPs play a central role in the photocatalytic reduction of CO_2 to CO, facilitating heterolytic H_2 dissociation and generating a protonated/hydridic SFLP (HOH-Ti-[O]--Ti-H). These Ti^{3+} species are critical for the binding of CO_2 and the formation of a formic acid intermediate, which subsequently decomposes into CO and H_2O [27]. We have recently studied In_2TiO_5 as a photocatalyst with dual active sites for CO_2 photoreduction. This study also addresses the importance of Ti^{3+} in the efficient adsorption of CO_2 molecules, facilitating the conversion of CO_2 to CH_4. When exposed to light, the Ti^{3+} centres can be excited, transferring electrons to the adsorbed CO_2 molecules. This electron transfer process catalyses the reduction of CO_2 to hydrocarbon species. The Ti^{3+} centre effectively serves as a reducing agent by providing the required electrons for the CO_2 photoreduction reaction [24]. In our recent perspective article, we discussed various challenges in photocatalytic CO_2 reduction using amorphous materials, including light harvesting, variable coordination number (CN), and adsorption hapticity of CO_2 molecules [28].

In this study, we formed two (type—II) heterostructures using crystalline TiO_2 (C—TiO_2) and amorphous-TiO_2 (A—TiO_2) in combination with CdSe. The C—TiO_2/CdSe heterostructure has limited active sites for CO_2 adsorption, whereas A—TiO_2 has a significant number of active sites. The disordered surface structure and defective states of A—TiO_2 increase the concentration of CO_2 adsorption required for photoconversion. The outermost coated A—TiO_2 on CdSe with asymmetric electric fields acts as an active site for continuous protonation, leading to CH_4 production [29,30]. Furthermore, A—TiO_2 has inherent advantages, such as multiple scattering of incident light, reduced carrier diffusion distance, enriched reactants in the cavities, and a flexible structure for building highly efficient catalysts [31,32]. CdSe absorbs light and undergoes photoexcitation, which creates electron-hole pairs. The resulting excited charge carriers can undergo redox reactions and thus facilitate the initiation of various chemical processes. In addition, CdSe exhibits remarkable photostability, a key feature for long service life in application. To maintain their effectiveness, photocatalysts must be exposed to light for an extended period without significant degradation. Therefore, CdSe was selected as the photo-excited material for this study. Extended X-ray absorption fluorescence spectroscopy (EXAFS) analysis was used to investigate the photocatalytic material's oxidation states and radial distance changes before and after CO_2 photoreduction. An interesting phenomenon involving the coexistence of Ti^{3+} and Ti^{4+}

in A—TiO_2/CdSe was discovered. Density functional studies show that the amorphous structure in A—TiO_2 promotes the localisation of charges transferred from CdSe at coordinately unsaturated surfaces, resulting in favourable and reductive adsorption of CO_2 into its bent geometry.

To surpass the conventional photocatalytic activity, we can explore concentrated solar flux as an alternative means to enhance the rate of CO_2 photoreduction. A recent study by Xu *et al.* introduced the utilisation of the photothermal effect to enhance the conversion of CO_2 into CH_4 through a concentrated solar reactor. Their approach employed a titanium foam-based monolithic photocatalyst (TF@TNT/0.4CoO$_{x-0.1}$CuO). Notably, they increased the solar intensity from 400 to 4266 mW/m^2 and observed a remarkable 220-fold increase in CH_4 production. In light of these findings, our investigation delves into the impact of varying solar intensities on distinct heterostructure surfaces [33]. Moreover, *In situ* experiments using Diffuse Reflectance Infrared Fourier Transform Spectroscopy (DRIFTS) and EXAFS techniques revealed two distinct reaction pathways in these heterostructures. We believe the interaction between CO_2 molecules and the photocatalyst surface plays a significant role in controlling these pathways. The primary goal of this research is to develop a heterostructure with optimised surface properties that enhance light absorption and control the reaction pathways.

2. Experimental section

2.1. Synthesis of C-TiO_2/CdSe

We employed an impregnation process to synthesise C-TiO_2/CdSe. Initially, we combined anhydrous ethanol and DI water in a ratio of 1:0.8. Then, we added a specific amount of CdSe and 200 mg of C-TiO_2 to the mixture. The reaction mixture was vigorously stirred for 6 h. After that, we subjected it to centrifugation and dried it under vacuum at 90°C for approximately 10 h.

2.2. Synthesis of A-TiO_2/CdSe

To synthesise the material, we employed the self-assembly approach. Initially, we combined 1.5 mL of titanium isopropoxide with 20 mL of isopropyl alcohol and introduced a specific quantity of CdSe to ensure an even distribution. Subsequently, we added 200 μl of NH_3 solution and sonicated the sample for 30 minutes. Then, we refrigerated the solution for roughly an hour until it reached a temperature of approximately 15°C. After removing it from the refrigerator, we promptly supplemented the solution with DI water and stirred it for 8 h. Following this, we centrifuged the resultant sample and dried it under the same conditions as mentioned before. We thoroughly washed the sample multiple times with DI water to remove carbon contamination. A more illustrative comparison with the synthesis of C-TiO_2/CdSe is shown in Fig. S1 of the Supporting Information (SI).

2.3. Photocatalytic activity

We conducted photocatalytic activity measurements of our samples using a custom-built photoreactor (Details mentioned in experimental section SI). Initially, we spread the photocatalyst evenly on a glass disc and sealed the reactor tightly using a vacuum to eliminate air or moisture. After that, we purged the reactor with CO_2 through a water bubbler, repeating the process five times before filling it with a CO_2/H_2O gas mixture. Irradiation of the reactor was carried out using a 100 W Xe arc lamp (AM 1.5 G, Oriel LCR 100, wavelength details as shown in Fig. S5a). The reaction conditions remained the same for the multi-sun effect experiment, but a 450 W Xe arc lamp (AM 1.5 G, Oriel Sol3A, wavelength details as shown in Fig. S5b) was used. We also examined the He/H_2O gas mixture for carbon contamination. To determine the evolution of CH_4, we used gas chromatography (GC) with a well-equipped flame ionisation detector (FID) and recorded the results. We

used $^{13}CO_2$ instead of $^{12}CO_2$ and gas chromatography-mass spectrometry (GC-MS) for the isotope test to assess the production $^{13}CH_4$.

2.4. Density functional simulation

All density functional calculations were conducted using Vienna ab initio Simulation Package (VASP) 5.4.1 [34–36]. The Perdew-Burke-Ernzerhof (PBE) functional [37] was selected for an exchange-correlation functional and the DFT-D3 method for dispersion energy correction [38]. The pseudopotentials were provided by the project-augmented wave (PAW) method [39]. The kinetic energy cutoff for the plane wave basis set was set as 450 eV, and the Monkhorst-Pack $(3\times4\times1)$k grid was employed for the slab models. All of the structures were optimised until the energy difference between the last two steps was below 1 meV. An initial TiO_2 slab structure was modelled as a 3-layered anatase TiO_2 at (101) surface consisting of 72 atoms (24 Ti atoms and 48 O atoms) and 20-Å vacuum thickness. Amorphous TiO_2 and its heterostructure with CdSe were modelled by ab initio molecular dynamics and DFT optimisation as described in the SI with Fig. S6. During the optimisation, the bottom half layer of CdSe was fixed. Molecules were optimised in a $(30\times30\times30)$-Å^3 cubic box and gamma-point only calculations. Bader charge analysis developed by Henckelman's group [40] was performed for quantitative charge difference calculations. The geometry of structures and their charge density were visualised using VESTA 3.5.7 [41].

3. Results and discussion

3.1. Method development

The synthesis of CdSe nanocrystals was carried out at room temperature in an inert environment. Two heterostructures with CdSe were prepared using A—TiO_2 and C—TiO_2. The SI includes the synthesis scheme in Fig. S1. The impregnation method was used to prepare C—TiO_2/CdSe. In the impregnation method, the development of an electrostatic charge on the TiO_2 surface facilitated the deposition of CdSe on it. Subsequently, the sol-gel self-assembly technique was used to form A—TiO_2 on the CdSe. Ti—isopropoxide served as a precursor for titanium and underwent partial hydrolysis, leading to the production of self-doped Ti^{3+} in the amorphous phase. In addition, an NH_3 solution was used to control the formation of A—TiO_2 on the CdSe. The direct synthesis of A—TiO_2 on the surface of the CdSe leads to a strong interfacial interaction, while the impregnation method results in a relatively unstable interface. The C—TiO_2/CdSe interface forms uniformly as a heterostructure, while direct growth produces a defective interfacial heterostructure.

3.2. Optical and charge carrier properties

It is important to emphasise that light absorption in the C—TiO_2/CdSe system follows a specific pattern, as shown in Fig. 1a. When CdSe nanocrystals are deposited on C—TiO_2, the absorption of visible light increases. Controlling the concentration of CdSe is crucial, as excess can cover the TiO_2 surface, impacting CO_2 adsorption and charge carrier phenomenon. Fig. 1b shows the light absorption behaviour of A—TiO_2/CdSe, which is a non-uniform and unpredictable pattern. Nevertheless, the overall light absorption is increased by defective states within the material, decreasing the band gap. The Tauc plot analysis for band gap determination is shown in Fig. S7(a-d) and Table S1. The most effective samples for CO_2 photoreduction are band gaps of 2.64 eV and 1.65 eV in C—TiO_2/CdSe and A—TiO_2/CdSe, respectively. In the case of C—TiO_2/CdSe, increasing the CdSe concentration decreases the band gap. Photoluminescence (PL) was analysed with an excitation wavelength of 350 nm to understand charge separation and recombination. Fig. 1c show a correlation between the CdSe concentration and the PL intensity associated with C—TiO_2/CdSe. In particular, an increase in CdSe
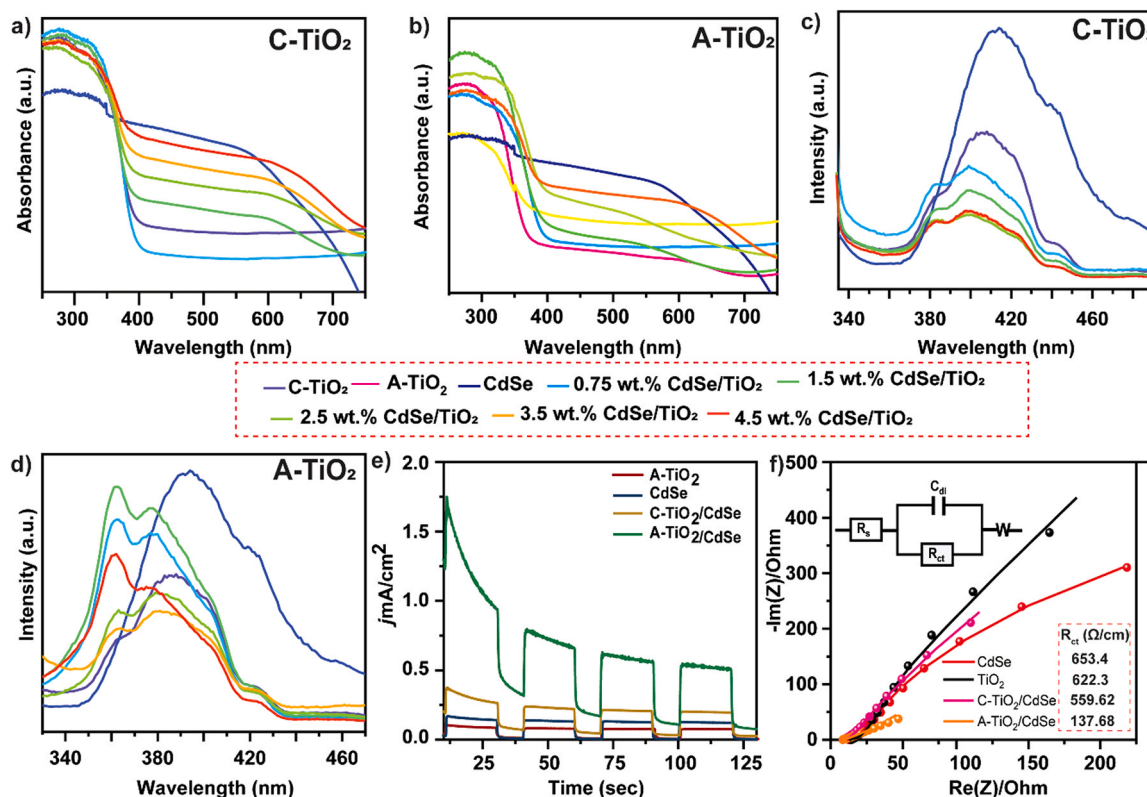

Fig. 1. Charge carrier dynamics analysis: DRS—UV—Vis analysis a) and b), PL analysis c) and d) of C—TiO_2/CdSe and A—TiO_2/CdSe, e) photoresponsivity and f) EIS analysis (inset shows the Randles circuit and R_{ct}).

concentration leads to a noticeable decrease in PL emission intensity. This observation indicates a dynamic electron migration phenomenon in which excited electrons move from the valence band (VB) of CdSe to the conduction band (CB) of TiO$_2$. The complexity of this interplay emphasises the critical importance of maintaining a precise concentration of CdSe to develop an efficient interface with C—TiO$_2$. Remarkably, the peak efficiency of the interface transition between CdSe and C—TiO$_2$ is reached at a concentration of 2.5 wt% CdSe. In contrast, when A—TiO$_2$/CdSe is exposed to the same excitation wavelength, Fig. 1d shows a different scenario characterised by defective energy states and random rearrangements at the interface between TiO$_2$ and CdSe. This phenomenon manifests as multiple energy state peaks indicating localised electronic states that facilitate charge transport through a hopping mechanism and generate thermal energy in amorphous materials. Interestingly, an effective interfacial heterostructure is formed at a concentration of 3.5 wt% CdSe. The resulting rapid decrease in emission spectra serves as a tangible indicator of the effectiveness of charge separation within the heterostructure [42]. This particular analysis sheds light on the complicated dynamics that govern the interplay between CdSe concentration and the assembly of effective interfacial heterostructures in C—TiO$_2$/CdSe and A—TiO$_2$/CdSe configurations. A PL density variation is shown in Figs. S8(a and b) shows an emission matrix diagram for optimised C—TiO$_2$/CdSe and A—TiO$_2$/CdSe.

Light emission intensity decreases as the effective charge transfer increases, and vice versa. As a result, A—TiO$_2$/CdSe show improved charge separation compared to C—TiO$_2$/CdSe. To better understand the behaviour of light-induced charge carriers, we conducted a photoresponsivity analysis, the experimental details of which are included in the SI. Fig. 1e illustrates that A—TiO$_2$/CdSe exhibit a higher current density than C—TiO$_2$/CdSe. Furthermore, we performed a Nyquist analysis to assess carrier mobility. It is worth noting that the A—TiO$_2$/CdSe heterostructure displays the lowest resistance, as depicted in Fig. 1f. In the case of amorphous materials, interparticle resistance plays a significant role. In Fig. 1f (inset), we used the so-called Randles circuit to simulate our data. This circuit consists of the parallel connection of two components: the charge transfer resistance (R_{ct}) and the interfacial capacitance (C_{dl}). R_{ct} and C_{dl} describe the movement of the Faraday current or the non-Faraday current through the interface. This circuit models the solid-liquid interface of catalysts, where one side is the catalyst electrode. In catalyst electrodes, R_{ct} is associated with electron transfer reactions such as charge transfer resistance within the catalyst through surface sites. The inset in Fig. 1f also shows the calculation of Rct and that the highest resistance is 653.4 Ω/cm for CdSe. In contrast, the A-TiO$_2$/CdSe sample has a lower resistance of 137.68 Ω /cm. This indicates that the electron transfer in A-TiO$_2$/CdSe is more effective than in the other samples due to its high number of surface active sites.

3.3. Structural and morphological characterisations

X-ray diffraction (XRD) analysis was used to study the changes in the structure of the photocatalysts. In the case of pristine C-TiO$_2$, we observed peaks at 2θ values, 25.30° (101), 37.89 ° (004), 48.12 ° (200), 53.96 ° (105), 55.03 ° (211) and 67.74 ° (213). These peaks indicate the anatase phase of TiO$_2$, as previously reported [43]. Moreover, the XRD pattern of CdSe showed distinct peaks at 2θ values of 25 °, 45 ° and 50 °, corresponding to (002), (110) and (112), respectively. According to previous studies, these peaks indicate an α-blend structure of the CdSe [44].

The formation of a heterostructure from the combination of C—TiO$_2$ and CdSe is shown in Fig. S9a. When the CdSe was deposited on TiO$_2$, the (004) peak disappeared, and the (105) and (211) peaks merged, which is clear evidence of the formation of a heterostructure. In contrast, the XRD pattern of the A—TiO$_2$/CdSe (Fig. S9b) showed a single wide peak between 10° and 40°, confirming the dominance of A—TiO$_2$, while no peaks were observed for the CdSe. It is, therefore, proven that the CdSe are coated with A—TiO$_2$. To analyse the chemical composition of

the TiO$_2$/CdSe, X-ray photoelectron spectroscopy (XPS) was used.

XPS was used to analyse the chemical composition of the TiO$_2$/CdSe. Fig. S10a shows the wide spectrum of TiO$_2$, and Fig. S10b shows the high-resolution XPS peaks (HR—XPS) at 458.68 and 464.42 eV, corresponding to Ti 2p$_{3/2}$ and Ti 2p$_{1/2}$, respectively. The O 1 s peaks (Fig. S10c) at 529.35, 529.87 and 530.34 eV are attributed to Ti—O—Ti, lattice oxygen and a hydroxyl group on the surface, respectively [45]. In their initial state, the CdSe have two different configurations of Cd atoms: on the surface and in the inner crystal lattice [46]. The surface Cd state plays a role in the H$_2$O adsorption sites [47]. Fig. S11a shows the wide spectrum of CdSe, and Fig. S11b shows Cd 3d$_{5/2}$ and Cd 3d$_{3/2}$ binding energies of 404.95 and 411.72 eV, respectively. In addition, Se is detected at 52.97 (3d$_{5/2}$) and 53.62 eV (3d$_{3/2}$), as shown in Fig. S11c. The ratio of Se atoms at the inner and outer surfaces is similar, indicating minimal defective states at Cd and Se sites in pristine CdSe. Fig. S12a and b shows a wide spectrum of C—TiO$_2$/CdSe and A—TiO$_2$/CdSe, respectively.

The Ti 2p peaks are observed at 457.57 and 463.24 eV, which can be attributed to Ti^{3+} defect states (Fig. 2a). In addition, O 1 s exhibits peaks at 528.73, 529.27, 529.71 and 531.05 eV corresponding to Ti—O—Ti, lattice oxygen (Ti^{4+}), hydroxyl group and lattice oxygen (Ti^{3+}), respectively (Fig. 2b). Furthermore, the presence of Ti^{3+} can be attributed to a lower binding energy resulting from the distortion caused by the additional electrons within the TiO$_2$ lattice [48,49]. In Fig. 2c, we observe an increase in the surface-to-internal Cd ratio in C-TiO$_2$/CdSe. Consequently, as the number of Cd sites on the surface rises, so does the number of dangling bonds. Fig. 2d illustrates the apparent interaction between the surface and the internal components in the case of Se. This suggests significant interactions between the CdSe and A—TiO$_2$. As evidenced in Fig. S12b, the composition of the A—TiO$_2$/CdSe is noticeable through their wide XPS spectrum. The HR-XPS analysis of Ti 2p showed increased intensity attributed to Ti^{3+}. Consequently, the number of Ti^{3+} sites also increased (Fig. 2e). The lattice oxygen and hydroxyl groups on the surface, as shown in Fig. 2f, contribute to the adsorption of CO$_2$. Remarkably, the presence of A-TiO$_2$ on CdSe resulted in a decrease of Cd atoms on the surface but an increase of internal Cd sites (Fig. 2g). Interestingly, no observable distributions of surface or internal Se were detected, which can be attributed to the extended contact between CdSe and A-TiO$_2$ covering the active sites, as shown in Fig. 2h, i. Raman spectroscopy analysis performed to investigate stress and strain in the materials. Theoretically, A-TiO$_2$ peaks correspond to E$_g$ and A$_{1g}$, where E$_g$ stands for in-plane stretching, indicating an interaction between equatorial oxygen (O$_{eq}$—Ti—O$_{eq}$) and bending vibrations. A$_{1g}$ stands for O—O and a pure Ti—Ti bond [50]. Consequently, the stretching vibration was minimised from the plane of heterostructured C-TiO$_2$/CdSe, confirming the deposition of CdSe on TiO$_2$. Moreover, the A-TiO$_2$/CdSe heterostructure showed a decrease in out-of-plane stretching and an increase in in-plane stretching. This indicates that the direct growth of A-TiO$_2$ leads to a change in the lattice composition, thereby promoting material stretching. In addition, the A$_{1g}$ peak exhibited asymmetric broadening due to the presence of Ti^{3+} as active sites affecting the vibrations of the neighbouring O atoms in the lattice. The observations indicated two phonon vibrations in the pristine CdSe: surface optical modes and longitudinal optical phonons. These peaks were broadened due to phonon confinement and structural deformation of the CdSe lattice.

X-ray absorption fine structure (XAFS) experiments investigated the chemical environment, the active sites' oxidation states, and the CN within the heterostructure. Ti and Cd were considered as potentially active sites within this structure. Consequently, we provide a detailed investigation of the Ti K-edge and the Cd K-edge with experimental techniques described in SI. Fig. 3a compares the Ti K-edge between C—TiO$_2$/CdSe and A—TiO$_2$/CdSe. We analysed the pre-edge structure of the Ti K edge and found that P$_1$ and P$_2$ correspond to the exciton band and P$_3$ to the 1 s-3d transition, as shown in Fig. S13 [51–53]. In particular, the absence of P$_1$ in A—TiO$_2$/CdSe indicates a distortion of
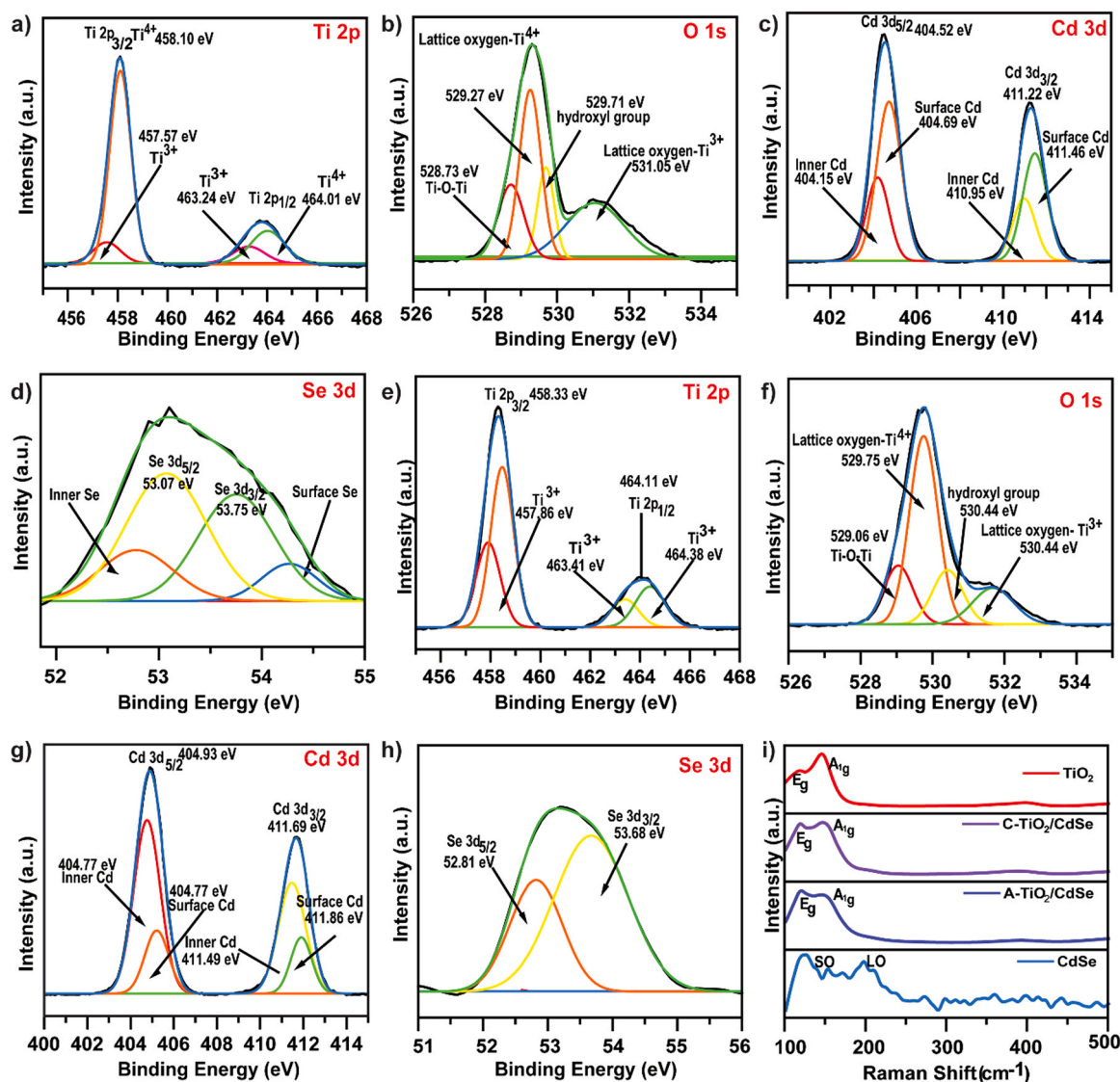
Fig. 2. Surface analysis: HR−XPS analysis a) Ti, b) O, c) Cd, and d) Se of C−TiO$_2$/CdSe and e) Ti, f) O, g) Cd, and h) Se of A−TiO$_2$/CdSe and i) Raman spectroscopy analysis.

the quadrupole transition. Moreover, the intensity of P$_2$ is more distinct in A−TiO$_2$/CdSe than in C−TiO$_2$/CdSe due to the formation of a distorted octahedral geometry and a tetrahedral geometry. C−TiO$_2$/CdSe shows a 1s-3d transition, although no octahedral distortion is observed. This observation confirms the presence of a Ti^{3+}/Ti^{4+} combination in A−TiO$_2$/CdSe. To confirm this, we compared the EXAFS with TiO$_2$ (Ti^{4+}), Ti$_2$O$_3$ (Ti^{3+}), TiO (Ti^{2+}) and Ti foil (Ti^0). It was found that the atomic vibrations observed in Ti$_2$O$_3$ are similar to those in A−TiO$_2$/CdSe. The lower magnitude of atomic vibrations in C−TiO$_2$/CdSe and A−TiO$_2$/CdSe can be attributed to nonlinear multiple scattering [54]. In Fig. 3b, we studied the Fourier transform (FT) of the EXAFS analysis, which shows an overall significant peak at 1.94 Å for Ti−O and 3.20 Å for Ti−Ti. However, smaller peaks are observed for C−TiO$_2$/CdSe and A−TiO$_2$/CdSe, as nonlinear backscattering limits the extent of atomic oscillation. This finding confirms that the atomic environment of the heterostructure changes significantly during its formation. We also compared the radial distances of A−TiO$_2$/CdSe and C−TiO$_2$/CdSe with those of TiO, Ti$_2$O$_3$ and TiO$_2$. In Fig. 3c, we also compared the k^3-weighted EXAFS of C−TiO$_2$/CdSe and A−TiO$_2$/CdSe and found that the atomic absorption intensities in A−TiO$_2$/CdSe are lower than in C−TiO$_2$/CdSe. This indicates that the wave phase of the atoms is out of phase. This work demonstrates that nonlinear

backscattering is more prominent in amorphous materials than crystalline ones.

This work demonstrates that nonlinear backscattering is more prominent in amorphous materials than crystalline ones. We also investigated the XAFS of the Cd K-edge in a heterostructure and compared it with Cd foil and synthesised CdSe nanocrystals. Fig. 3d shows that the oscillations are minimised in the C−TiO$_2$/CdSe- and A−TiO$_2$/CdSe due to the heterostructure and the presence of amorphous defects. Further analysis of Cd foil's FT reveals that the radial distance between Cd−Cd atoms is 2.94 Å. CdSe reduces this radial distance by 0.32 Å, confirming the formation of Cd−Se bonds. Interestingly, A−TiO$_2$/CdSe (2.70 Å) and C−TiO$_2$/CdSe (2.68 Å) slightly increase the Cd−Se radial distance, indicating a strong interaction between TiO$_2$ and CdSe (Fig. 3e). The k^3-weighted EXAFS spectrum of Cd is depicted in Fig. 3f. In this spectrum, CdSe exhibits significant oscillation at high k-space (ranging from 6 to 9 Å^{-1}) due to the distance between the wave phases of the absorbing and scattering atoms. As disorder within the heterostructure increases, the oscillation amplitude decreases.

To investigate oxygen vacancies in A−TiO$_2$/CdSe, electron paramagnetic resonance (EPR) spectroscopy was employed. A prominent peak at g = 2.04 suggests electron capture at oxygen vacancies (Fig. S14) [55–57]. Additionally, EPR analysis after the reaction did not reveal any
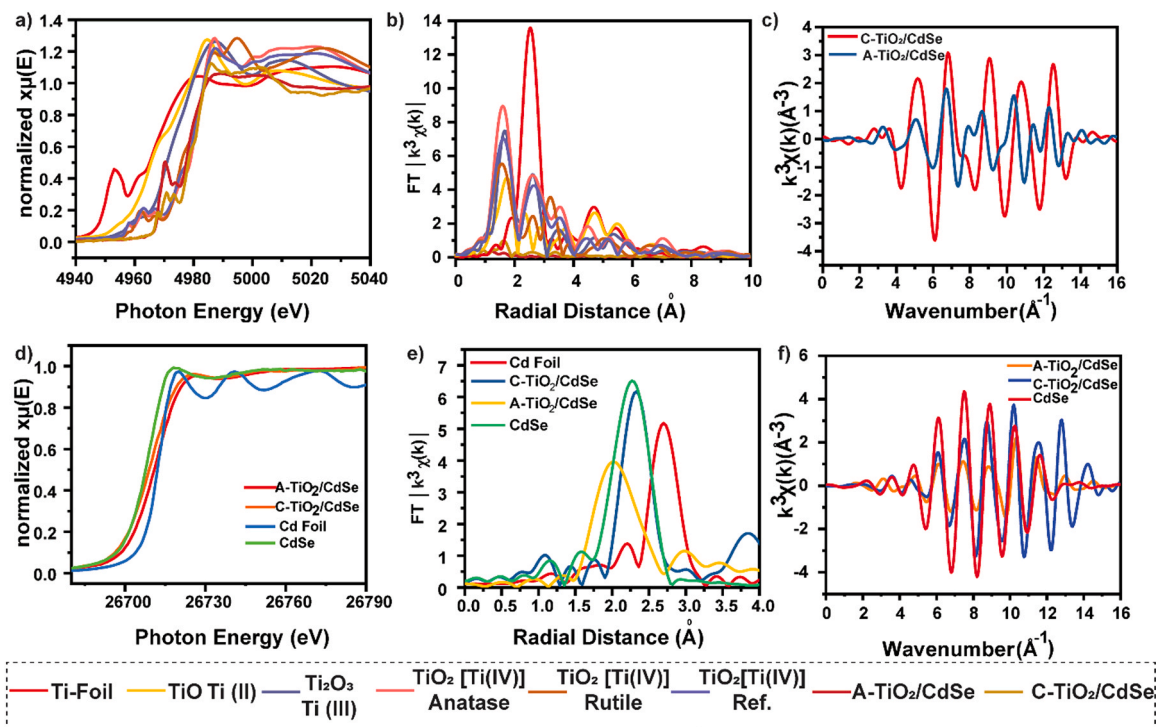
Fig. 3. Coordination state analysis of Ti and Cd: a) Ti K—edge EXAFS spectra, b) FT amplitude of TiO$_2$ polymorphism compared with C—TiO$_2$/CdSe and A—TiO$_2$/CdSe, c) Ti k^3—weighted EXAFS spectra of C—TiO$_2$/CdSe and A—TiO$_2$/CdSe, d) Cd K—edge EXAFS spectra e) FT amplitude of Cd and f) Cd k^3—weighted EXAFS spectra of C—TiO$_2$/CdSe and A—TiO$_2$/CdSe compared with CdSe.
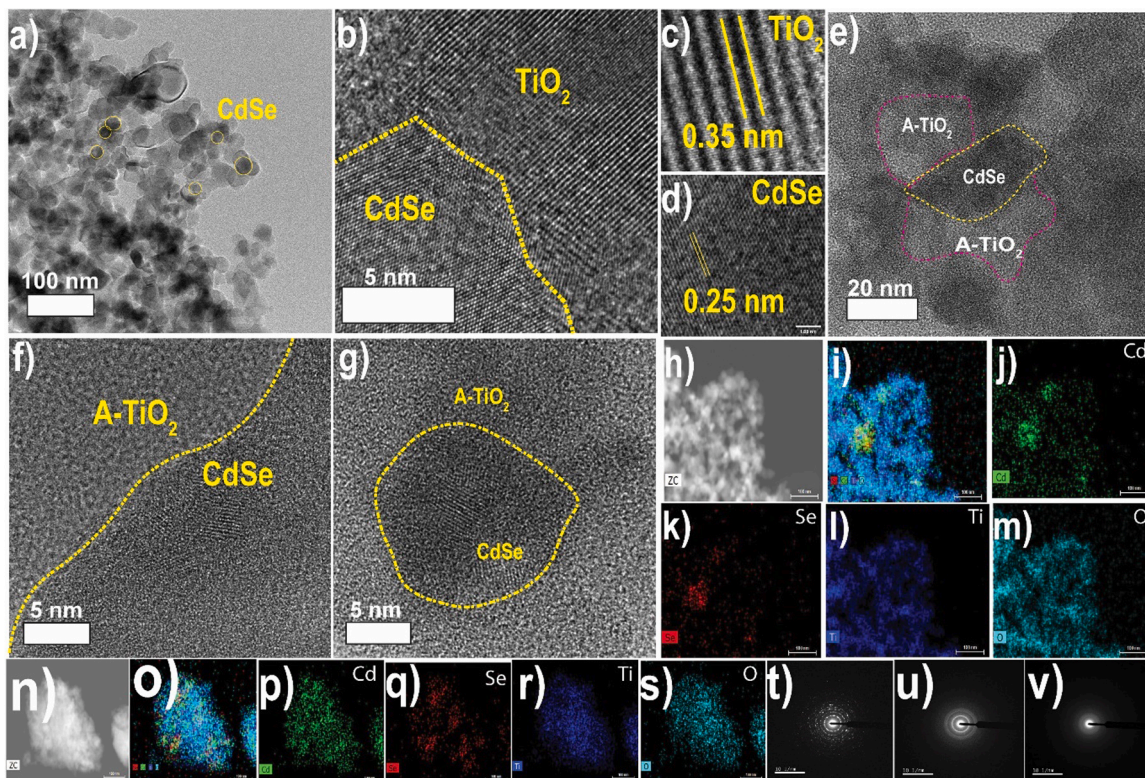

Fig. 4. Nanostructural characterisations: TEM of a) C—TiO$_2$/CdSe, b) HRTEM shows that the formation of heterostructure between C—TiO$_2$ and CdSe, c) and d) demonstrates the distinct d—spacing for C—TiO$_2$ and CdSe, respectively, e) TEM of A—TiO$_2$/CdSe where the coloured dotted line illustrates the A—TiO$_2$ and CdSe, f) and g) HRTEM shows that the formation of heterostructure between A—TiO$_2$/CdSe, h)-m) shows the elemental mapping of Cd, Se, Ti and O, n)-s) shows the elemental mapping of Cd, Se, Ti and O, t) selective area of the diffraction pattern attribute crystalline for C—TiO$_2$/CdSe, u) partially diffused ring due to the A—TiO$_2$ and crystalline CdSe; however, v) it shows the entire diffused ring due to the presence of A—TiO$_2$.

peaks, confirming the involvement of captured electrons in CO_2 photo-reduction. Brunauer–Emmett–Teller (BET) analysis was conducted to understand the active surface area and CO_2 adsorption capacity. A—TiO_2/CdSe exhibited a larger active surface area than C—TiO_2/CdSe, which is attributed to dangling bonds on the surface of A—TiO_2. Fig. S15a illustrates that CdSe inhibits active sites on C—TiO_2. Moreover, CO_2 uptake, as shown in Fig. S15b, is significant for A—TiO_2/CdSe due to their extensive surface area. Notably, A—TiO_2/CdSe exhibit a broad pore size distribution, ranging from mesoporous to microporous, while TiO_2, CdSe, and C—TiO_2/CdSe are primarily mesoporous (Fig. S15c).

We conducted scanning electron microscopy (SEM) analysis of the CdSe nanocrystals to examine their surface morphology, as depicted in Figs. S16(a,b). Fig. S16b demonstrates the presence of porosity and a particle size distribution ranging from 20 to 30 nm. Elemental mapping in Fig. S16(c,d) indicates a homogeneous distribution of Cd and Se, with corresponding quantitative data in Table S2. Figs. S16(e,f) reveals that the porous nature of TiO_2 remained unchanged after the deposition of CdSe on C—TiO_2. However, the particle size increased, and TiO_2 parti-cles aggregated upon CdSe deposition—element mapping in Figs. S16(g, h) and quantitative measurements in Table S3 support these observa-tions. In the case of A—TiO_2/CdSe, it is evident that TiO_2 completely covers the CdSe, rendering them invisible at the surface, as illustrated in the SEM images in Figs. S16(o,p) and the corresponding elemental mapping in Figs. S16(q-t) and quantitative analysis in Table S4.

High-resolution transmission electron microscopy (HRTEM) studies confirmed that the CdSe possesses an average size of 5.24 nm (Fig. S17i). Figs. S17(a-c) reveal that the CdSe were synthesised without a capping agent, leading to agglomeration. The 0.25 nm d-spacing observed aligns with previous reports on CdSe [58].

Furthermore, Fig. S17(d) illustrates the CdSe nanocrystal arrays at increasing magnification, with Cd atoms marked in yellow and Se atoms in red—elemental mapping in Figs. S17(e-h) demonstrates a consistent distribution of Cd and Se throughout the nanocrystals. Fig. 4a and b depict the well-distributed placement of CdSe over the TiO_2 nano-particles, confirming the formation of a heterostructure at the grain boundaries. Consequently, the alignment of two distinct d-spacings was observed. In Fig. 4c and d, TiO_2 and CdSe exhibit d-spacings of 0.35 nm and 0.25 nm, respectively. Fig. 4e provides strong evidence that A—TiO_2 effectively envelops the CdSe in the case of A—TiO_2/CdSe. Fig. 4f and g reveal that the heterostructure formed between A—TiO_2 and crystalline CdSe comprises two distinct regions. The presence of A—TiO_2 on the CdSe makes it challenging to differentiate between the particles; how-ever, it is confirmed that both phases coexist.

Furthermore, elemental mapping reveals a random distribution of Cd, Se, Ti, and O, indicating a non-uniform interfacial arrangement (Fig. 4(h-m) and (n-s)). Supplementary TEM and HRTEM images can be found in the SI in Fig. S18(a-l). The non-uniform growth of A-TiO_2 is clearly visible in these TEM and HRTEM images, as shown in Fig. S18(d-l). This non-uniform growth of A-TiO_2 on CdSe effectively leads to numerous active Ti^{3+} sites on A-TiO_2/CdSe. Fig. 4(t-v) analyses the se-lective area electron diffraction (SAED) patterns of A—TiO_2, C—TiO_2/CdSe, and A—TiO_2/CdSe. Diffuse rings are observed in A—TiO_2/CdSe due to the highly disordered atomic arrangement in A—TiO_2, whereas C—TiO_2/CdSe exhibits a crystalline appearance. A diffuse crystallo-graphic pattern is observed when the heterostructure between A—TiO_2 and CdSe is formed.

4. Sunlight—driven photocatalytic CO_2 reduction

The performance of photocatalytic CO_2 reduction using C—TiO_2/CdSe and A—TiO_2/CdSe was evaluated in the gas phase (Fig. S4). Varying the concentration of CdSe impacted light absorption and charge carrier dynamics. Optimised concentrations of 0.75, 1.5, 3.5, and 4 wt% CdSe were determined to increase CO_2 photoreduction. C—TiO_2/CdSe, characterised by well-organised interfacial arrangements at the junc-tion, exhibited an increased CO_2 photoreduction rate with higher concentrations of CdSe.

Fig. 5a illustrates a cumulative yield of 2.08 μmol/g for CH_4 evolu-tion after a 12 h reaction with 3.5 wt% of CdSe on the C—TiO_2 surface. However, as the deposition of CdSe on C—TiO_2 increased, there was a noticeable decrease in CH_4 evolution. A—TiO_2/CdSe, employing a lower concentration of CdSe (0.75 wt%), demonstrated a significantly higher CH_4 yield (6.30 μmol/g), as shown in Fig. 5b. This result suggests that intense contact was established due to the direct growth of A—TiO_2 on the CdSe, facilitating efficient charge dynamics. Comparing A—TiO_2/CdSe with various interfacial ratios of CdSe (0.75, 1.5, 2.5, 3.5, and 4.5 wt%) to C—TiO_2/CdSe, the CO_2 reduction rate increased by factors of 33.15, 7.91, 7.67, 2.05, and 2.70, respectively. This enhanced CH_4 yield in A—TiO_2/CdSe is primarily attributed to increased CO_2 adsorp-tion, localised charge transfer, and electronegative differences formed at the interface, owing to the highly disordered atomic structure and non-uniform electric field distribution.

Additionally, the heterointerface of A—TiO_2/CdSe on the outermost A—TiO_2 layer helped reduce charge resistance due to localised electronic states (trapping energy states). To assess the stability of the photo-catalyst, consecutive photocatalytic reaction cycles were conducted, with the photocatalyst regenerated under an Ar gas stream with constant heating (details provided in the SI). CH_4 evolution was monitored every 6 h. By the third cycle (18 h), C—TiO_2/CdSe nearly matched the CH_4 yield in the first cycle, as shown in Fig. 5c. However, over time, the CH_4 evolution yield experienced a significant decrease, possibly due to strong adsorption of reaction intermediates, making desorption difficult and leading to active site deactivation. In contrast, A—TiO_2/CdSe demonstrated exceptional stability for up to 24 h, as depicted in Fig. 5d. While CH_4 evolution decreased during the second cycle compared to the third cycle, subsequent cycles exhibited a renewal of active sites. Notably, a 60% CH_4 yield was achieved during the fifth cycle, followed by a decline in CH_4 production. A—TiO_2/CdSe facilitated the restoration of Ti^{3+} active sites and oxygen vacancies through photocatalyst regen-eration. The XRD patterns were analysed before and after the CO_2 photoreduction reaction, revealing no significant changes (Figs. S19a and b). An isotope test was conducted to confirm the source of CO_2, where $^{12}CO_2$ was replaced with $^{13}CO_2$. The observation of the $^{13}CH_4$ peak confirmed that CH_4 production resulted from CO_2 photoreduction (as shown in Fig. S20). Controlled experiments using He/H_2O instead of a CO_2/H_2O mixture further confirmed that the reaction product resulted from photocatalytic CO_2 reduction, with minimal carbon contamination observed (Fig. S21). A half-oxidation reaction, $2 H_2O \rightarrow O_2\uparrow + 4 H^+ + 4 e^-$ was undertaken, while using C-TiO_2/CdSe and A-TiO_2/CdSe as a photocatalyst. This study focused on oxygen evolution, as depicted in Fig. S22. The process of H_2O oxidation facilitates the production of protons (H^+). Experimental oxygen evolution occurred under conditions similar to CO_2 photoreduction. A comparative analysis of the observed O_2 evolution and the standard retention time of O_2 gas in GC was con-ducted. This analysis confirmed that the half-reaction takes place during CO_2 photoreduction.

4.1. Multi—solar photon flux—driven photocatalytic CO_2 reduction

The photon flux, representing the number of photons striking a surface within a specific period, plays a crucial role in photocatalysis. The energy that reaches the surface per unit time can be calculated by multiplying the photon flux by the energy carried by each photon. When the photon flux increases, more photons interact with the photocatalyst material, resulting in greater availability of electrons for photocatalytic reactions. Furthermore, an increase in solar flux elevates the reaction temperature, allowing for both photon and thermal effects. Conse-quently, the chemical kinetics of CO_2 reduction can be influenced.

In our experiments, we conducted multi-solar photon flux photo-catalytic CO_2 reduction using C—TiO_2/CdSe- and A—TiO_2/CdSe-as a photocatalyst, observing the evolution of CH_4 (detailed experimental procedures in SI). Fig. 5e demonstrates that for C—TiO_2/CdSe, CO_2
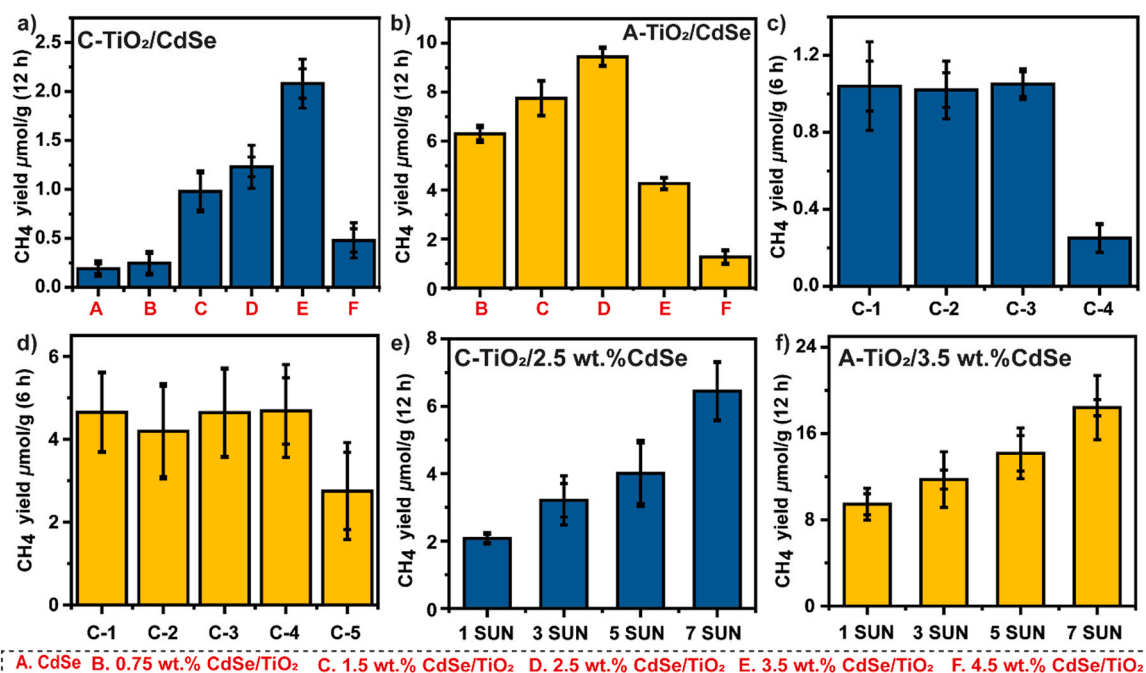
Fig. 5. The photocatalytic performance of CO_2 reduction: a) and b) show that photocatalytic CO_2 reduction under 1 Sun condition, c) and d) demonstrated the photocatalyst stability for C—TiO_2/CdSe and A—TiO_2/CdSe respectively, e) and f) photocatalytic under multi—solar photon flux.

photoreduction increased with higher solar radiation intensity. Specifically, 3.21, 4.01, and 6.45 μmol/g of CH_4 were produced for 3, 5, and 7 suns, respectively. These CH_4 yields were 1.54, 1.92, and 3.10 times higher for 3, 5, and 7 suns, respectively, compared to 1 Sun illumination. In contrast, for A—TiO_2/CdSe (as shown in Fig. 5f), CH_4 production was observed at approximately 11.72, 14.16, and 18.4 μmol/g for 3, 5, and 7 suns, respectively. These yields increased by 0.80, 1.50, and 1.94 times for 3, 5, and 7 suns, respectively, compared to 1 Sun illumination.

During the multi-sun test, the temperature of the photocatalyst was not regulated, while the 1-sun test was conducted at room temperature. The reactor temperatures of the reaction are recorded in Table S5. This data reveals that the maximum temperature reached by C—TiO_2/CdSe at 7 suns is 2.32 times higher than at room temperature. Similarly, amorphous materials like A—TiO_2/CdSe exhibit a thermal energy increase of 2.8 times compared to room temperature due to enhanced light scattering. Localised electronic states can also trap electrons and generate thermal oscillations, potentially reducing the semiconductor band gap and broadening the light absorption spectrum. This can also lead to increased charge recombination, reducing catalytic efficiency. However, our catalyst exhibits no noticeable thermal effects even with a temperature increase to 70 °C. As a result, our investigation into photocatalytic CO_2 reduction indicates a primary reliance on the photon effect rather than the thermal effect. In the thermally assisted photocatalysis mode, the primary driving force of the reaction is the electrons generated by light. In this mode, the temperature rises from the heat the catalyst releases after light absorption or external heat input. However, this temperature increase is insufficient to reach the light-out temperature characteristic of thermocatalysis. It is important to note that the catalyst itself lacks thermocatalytic activity. Instead, the thermal energy facilitates the photocatalytic process by lowering the apparent activation energy of photocatalysis. This thermal enhancement increases the mobility of charge carriers and facilitates the mass transfer of reactants, contributing to the overall efficiency of the photocatalytic reaction [59].

To gain a broader perspective on photocatalytic CO_2 reduction driven by multi-sun photon flux, we reviewed previous studies on CO_2 photoreduction using concentrated sunlight, as summarised in Table S5. It is important to note that the reaction conditions and pathways investigated in these studies varied. Nonetheless, two primary findings

emerge from these studies: firstly, a higher solar flux intensity does not necessarily result in a proportional increase in hydrocarbon production, and secondly, intense solar flux can induce thermal vibration, which may decrease hydrocarbon yields. Therefore, optimising these two things will further enhance CO_2 photoreduction.

5. Insights into the photocatalytic CO_2 reduction mechanism

We conducted an ultraviolet and X-ray photoelectron spectroscopy (UPS-XPS) analysis to understand the thermodynamic barriers involved in the CO_2 photoreduction reaction to determine the band edge position for TiO_2, CdSe, C—TiO_2/CdSe, and A—TiO_2/CdSe. The adequacy of the band gap was attributed to the CO_2 photoreduction reaction in these materials. Fig. S23 illustrates the energy cutoff (E_c) edges for these materials, which were found to be 16.53 (A-TiO_2), 15.82 (C-TiO_2), 17.82 (CdSe), 16.72 (C—TiO_2/CdSe), and 18.14 eV (A—TiO_2/CdSe), respectively. Additionally, the VB positions (E_{VB-XPS}) for these materials were determined to be 2.41 (A-TiO_2), 2.09 (C-TiO_2), 1.97 (CdSe), 1.16 (C—TiO_2/CdSe), and 1.96 eV (A—TiO_2/CdSe). Band gap calculations were employed to determine the CB for all samples, revealing a shift to a negative potential value after the formation of the heterostructure. As demonstrated in Fig. S24, the heterostructure development indicates that both materials are thermodynamically favourable for reducing CO_2.

We utilised *In situ* XAFS to gain insight into the material modifications, including CN, oxidation states, and radial distance before and after CO_2 photoreduction(Fig. S3). EXAFS analysis of C—TiO_2/CdSe indicated octahedral geometry, while A—TiO_2/CdSe displayed tetrahedral geometry. No significant changes were observed after the reaction (Fig. 6a and b). Further analysis revealed that the radial distance of the Ti—O shell in C—TiO_2/CdSe initially measured 1.96 Å, which is comparable to 1.95 Å after the reaction (as shown in Fig. 6c). Conversely, in A—TiO_2/CdSe, the radial distance of Ti—O was initially 2.15 Å and decreased to 1.96 Å following CO_2 photoreduction (Fig. 6d). This suggests that an electron was localised to Ti^{3+} in the TiO_2 lattice, as evidenced by the increase in the first shell of Ti—O. During the photocatalytic CO_2 reduction reaction, Ti^{3+} species interacted with holes and facilitated the transfer of electrons from A—TiO_2 to CO_2 molecules. Additionally, Ti k^3—weighted scattering was analysed before
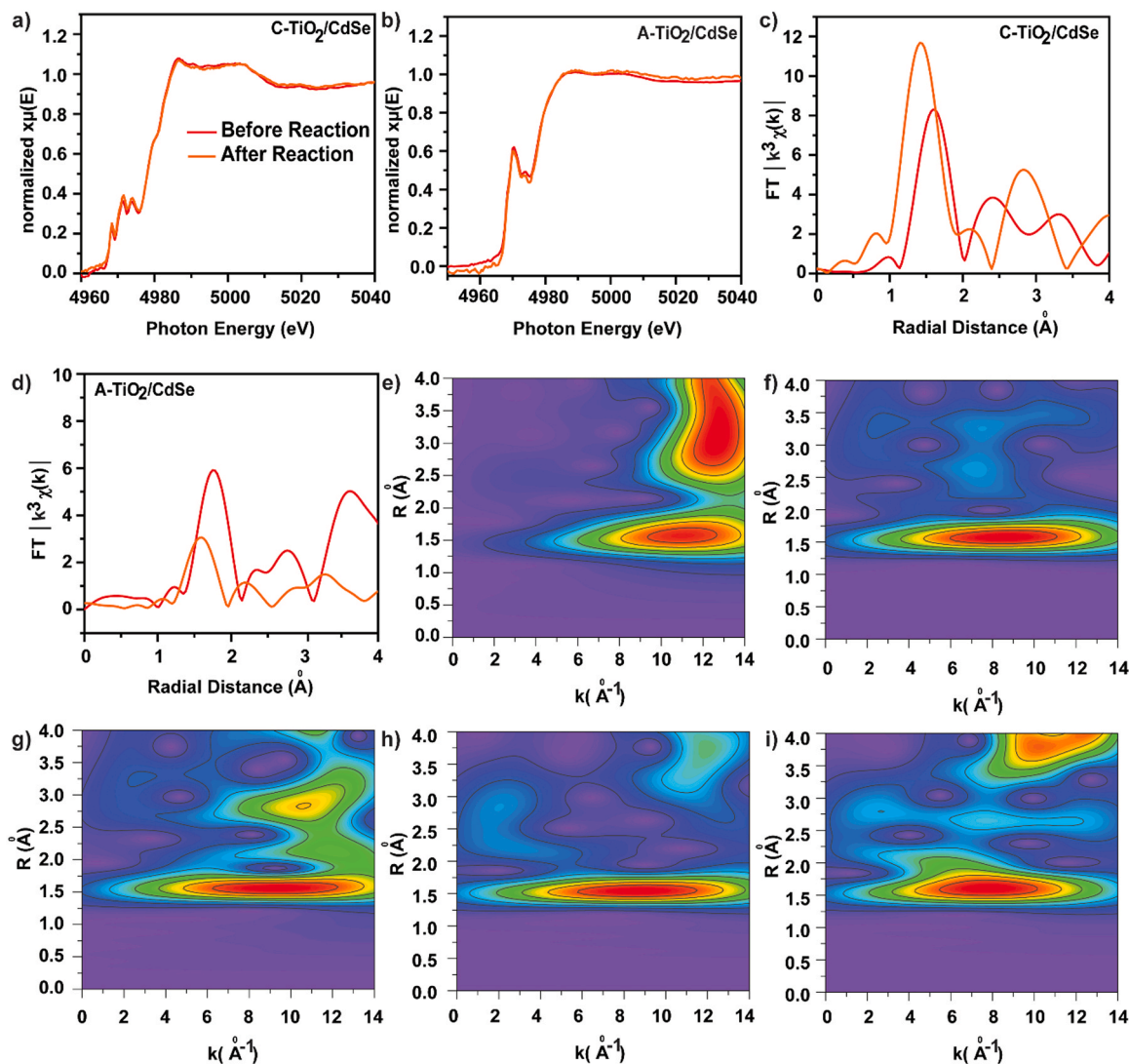
Fig. 6. Coordination state analysis of Ti^{3+}/Ti^{4+} before and after CO_2 photoreduction: a) and b) Ti K—edge EXAFS spectra before and after reaction, c) and d) FT amplitude of change in the radial distance of Ti—O before and after reaction, WT plots: e) C—TiO$_2$, f) before the reaction (C—TiO$_2$/CdSe) and g) after the reaction, h) and i) are similar before and after reaction for C—TiO$_2$/CdSe.

and after the reaction.

In the case of C—TiO$_2$/CdSe, scattering oscillations were unaffected at a lower k^3-weighted, but significant changes were observed at a higher k^3-weighted, indicating a unique coordinating environment. The CNs before and after the reaction were 3.35 and 3.60, respectively (Fig. S25a). However, σ^2 remained unchanged, indicating that atomic spacing disorder did not change. A—TiO$_2$/CdSe displayed significant changes in the k^3-weighted oscillations at lower k-space after the reaction, as shown in Fig. S25b, suggesting alterations in the surrounding coordination environment. The CN changed from 3.38 to 3.80 before and after the reaction. Furthermore, Ti^{3+} and Ti^{4+} coexistence shifted towards Ti^{4+} after the reaction, as indicated by the changes in the Ti—O peak distribution.

Simulation analyses using high-resolution wavelet transform (WT) were performed in both k-space and R-space. The Ti—O and Ti—Ti bond oscillation intensities in anatase TiO$_2$ were resolved (Fig. 6e). Significant changes were observed in the Ti—Ti oscillations after forming the C—TiO$_2$/CdSe heterostructure (Fig. 6f). The analysis of alterations following CO_2 photoreduction revealed oscillations at higher R (Fig. 6g), indicating that the Ti^{3+}/Ti^{4+} mixture shifted towards Ti^{4+}. In A—TiO$_2$/CdSe, multiple overlapping oscillations were observed due to the formation of a low-symmetry complex (Fig. 6h). After the reaction,

intensity distribution shifted to a higher R and lower k-space (Fig. 6i), suggesting that Ti^{3+} and Ti^{4+} coexist. The ratio of Ti^{3+} to Ti^{4+} remained relatively stable, indicating that A—TiO$_2$/CdSe were not immediately deactivated after the reaction.

Furthermore, we analysed the Cd K-edge both before and after the reaction. To assess the Cd K-edge in the XANES analysis, we compared it before and after the reaction with $CdCO_3$ and $Cd(OH)_2$ for the possible formation of hydroxides and carbonates on the CdSe surface. Fig. S30a reveals that C—TiO$_2$/CdSe exhibited a more significant shift in photon energy after the reaction, suggesting the formation of CdO due to Cd oxidation. This reaction was attributed to the highly dynamic nature of Cd deficiencies in the presence of H_2O. However, there were no observable changes in the conversion from Cd to $Cd(OH)_2$ and $CdCO_3$. In contrast, A—TiO$_2$/CdSe displayed a reduction in photon energy shift after the reaction (Fig. S30b), indicating the formation of $Cd(OH)_2$ and a slight intensification of the reaction. This observation further suggests that the shift in the d-band centre of Cd enhances the adsorption of H* and boosts photoreduction activity [60,61]. In the FT analysis of Cd, we observed that the radial distance of CdSe in C—TiO$_2$/CdSe decreased from 3.67 Å before the reaction to 3.43 Å after the reaction (Figs. S31a and b). On the other hand, the radial distance of CdSe in A—TiO$_2$/CdSe increased from 3.52 Å before the reaction to 3.56 Å radii after the

reaction. This change contributed to the formation of $Cd(OH)_2$. Additionally, the change in CN from 2.70 to 2.57 confirmed the upshift of the d-band centre of Cd, attributed to the transfer of electrons from Ti^{3+} to CdSe. We also compared the FT values of $Cd(OH)_2$ and $CdCO_3$ for each heterostructure (Fig. S32) and did not find an identical signature between heterostructures containing $Cd(OH)_2$ and $CdCO_3$. Moreover, we analysed the Cd k^3−weighted in C−TiO_2/CdSe and A−TiO_2/CdSe, as illustrated in Figs. S33(a, b). Following the reaction, the previously indirect oscillation absorption became noticeably more distinct, indicating an alteration in the immediate neighbouring coordination environment. We used WT plots to replicate backscattering oscillations, which enhanced the resolution (Figs. S34(a-e)). The heterostructures formed by C−TiO_2 and CdSe exhibited changes in oscillations in lower k and

R-spaces, indicative of nonlinear scattering in k-space. The asymmetry in the oscillation of A−TiO_2 resulted from the non-uniform dispersion of electrons at the interface. This shift in the d-band centre facilitated effective charge transfer due to the disparity in electron density. All fitting models and structural data generated from the fittings are included in the SI, including Table S7 and Figs. S26-S29, S35–S39.

The temperature-programmed desorption (TPD) of CO_2 was studied to investigate surface reactions and interactions between CO_2 and the photocatalyst (Fig. 7a). The CO_2-TPD results showed three significant peaks in the A−TiO_2/CdSe and C−TiO_2/CdSe heterostructures, whereas TiO_2 and CdSe did not exhibit these peaks. These peaks corresponded to molecularly adsorbed CO_2 (75–180 °C), HCO_3^- or HCO_2^- (180–350 °C), and b−CO_3^{2-} (380–450 °C), representing weak, moderate, and strong
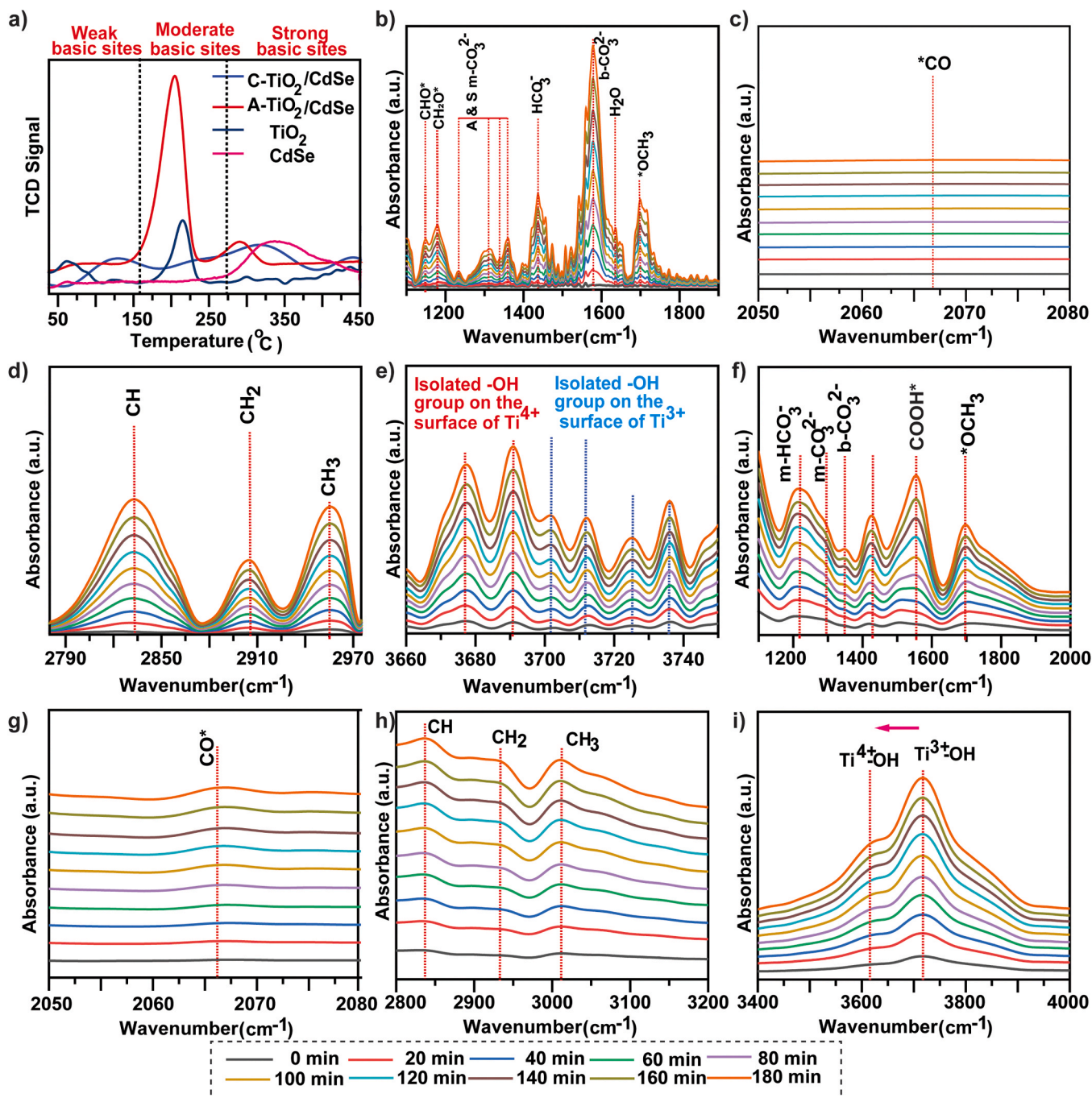

Fig. 7. Reaction mechanism analysis: a) TPD analysis of photocatalyst, In situ DRIFTS analysis under visible−light irradiation for b)-e) C−TiO_2/CdSe and f)−i) A−TiO_2/CdSe.

basic sites, respectively. A—TiO_2/CdSe primarily exhibited moderate basicity, allowing the formation of bicarbonate intermediates during the reaction. The predominant moderate basicity suggested that —OH groups covered the photocatalyst surface. Additionally, b—CO_3^{2-} species are formed by combining molecules with oxygen atoms or metals in the photocatalyst. These findings provide valuable insights into the surface interactions and modifications of the studied materials during the CO_2 photoreduction process.

Furthermore, *In situ* DRIFTS analysis was conducted to gain insights into the intermediate formation and reaction mechanisms during CO_2 photoreduction. Initially, the analyses were performed in the dark, and the SI includes experimental details(Fig. S2). Fig. S40 shows the molecular adsorption of CO_2, indicating that C—TiO_2/CdSe exhibited CO_2 molecule adsorption due to the photocatalyst's adequate defective states and oxygen vacancies. When solar light was irradiated onto the photocatalyst, the strong Lewis acidity and basicity of Ti^{4+} and oxygen led to the formation of CHO intermediates (observed at 1150.41 cm^{-1}). These CHO intermediates can further convert to CH_2O (observed at 1178.63 cm^{-1}) with additional electron/hydrogen ion (e^-/H^+) pairs. The protonation of a C atom was preferable to O, leading to the formation route depicted in Fig. 7b. The formation of —OCH_3 (observed at 1700 cm^{-1}) occurs when CH_2O accepts an e^-/H^+ combination. Additionally, these intermediate species correspond to asymmetric and

symmetric m—CO_3^{2-} peaks (observed between 1233.40 and 1361.20 cm^{-1}). A peak at 1646.37 cm^{-1} corresponding to H_2O formation was observed, indicating no CO production in this C—TiO_2/CdSe heterostructure (Fig. 7c). Furthermore, symmetric and asymmetric stretching vibrations of CH, CH_2, and CH_3 were detected at 2832.81, 2905.63, and 2954.86 cm^{-1}, respectively (Fig. 7d). The presence of CdSe on the TiO_2 surface, providing an active site of Cd^{2+}, led to the isolation of OH groups (Fig. 7e), as confirmed by EXAFS analysis. In A—TiO_2/CdSe, the CH_4 cycle was observed, and the photocatalyst was not immediately deactivated, indicating the CH_4 cycle and photocatalyst site regeneration. CO_2 molecules were found to bind strongly to Ti^{3+}, and upon light irradiation, Ti^{3+} acquired photogenerated electrons, which readily transferred to the LUMO of CO_2 molecules.

At 1553.32 cm^{-1}, the addition of e^-/H^+ pairs produced a COOH group, which further bonded with the monodentate carbon coordination mode, resulting in m—HCO_3^- at 1215.76 cm^{-1} and m—CO_3^{2-} at 1351.54 cm^{-1} (Fig. 7f). After accepting additional e^-/H^+, the COOH group underwent dehydration and produced CO*. If the binding energy between CO* and the photocatalyst was high, the intermediate CO could not be released as a product. As illustrated in Fig. 7g, CO was detected at 2068 cm^{-1}. Subsequently, hydration and dehydrogenation processes generated the aldehyde radical, which, in combination with three-step hydrogenation, produced the crucial intermediate *CH_3. Methoxy
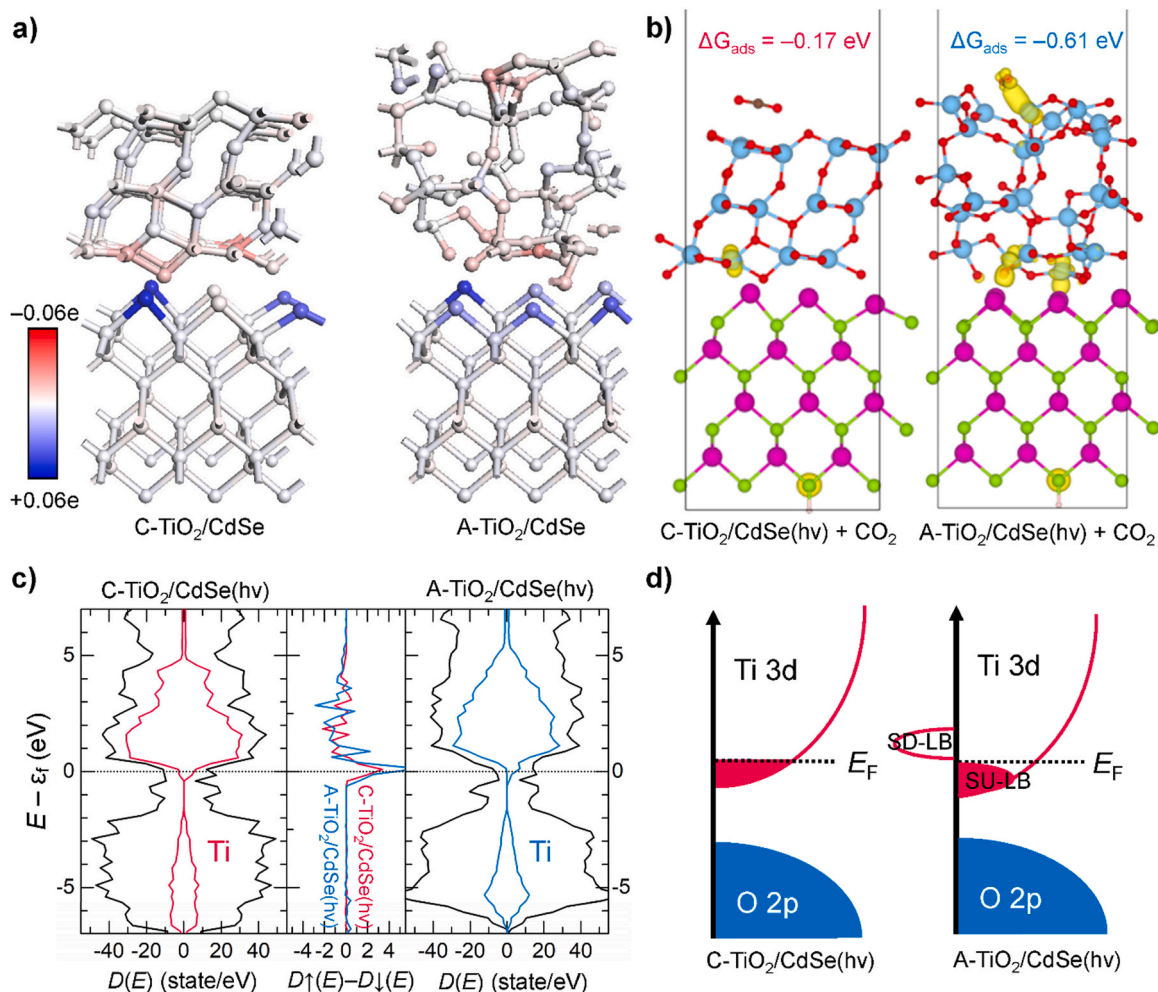

Fig. 8. Density functional analysis of C-TiO_2/CdSe and A-TiO_2/CdSe: a) Bader charge differences as coloured by charge scale in which red and blue represent electron accumulation and depletion up to 0.06e, respectively. b) Spin density analysis with CO_2 adsorption free energy (isosurface = 0.01 e/$Å^2$) after the photoexcited electron has been transferred by light absorption (hν). Atoms are coloured in light blue for Ti, red for O, magenta for Cd, green for Se and white for H, respectively. c) The total (black) and projected density of states of Ti (red and blue in C-TiO_2/CdSe on the left and A-TiO_2/CdSe on the right, respectively) and the difference between the density of up spin and down spin states $D_\uparrow(E) - D_\downarrow(E)$, on the middle, and d) the schematic explanation of the difference between the density of state of C-TiO_2/CdSe and A-TiO_2/CdSe after photoexcitation (hν).

(—OCH$_3$ at 1700 cm^{-1}) was another essential intermediate in this CO$_2$ photoreduction reaction cycle. Additionally, C—H stretching was detected at 2836.05−3004.49 cm^{-1} (Fig. 7h). A substantial amount of Ti^{3+} was obtained in the heterostructure, leading to the reaction of Ti^{3+} with H$_2$O, resulting in a hydroxyl group on its surface. Consequently, Ti^{3+}—OH changes to Ti^{4+}—OH at 3717 and 3615.62 cm^{-1} (Fig. 7i). These detailed spectroscopic analyses shed light on the complex intermediate formation and reaction pathways during CO$_2$ photoreduction on the studied photocatalysts.

The photocatalytic properties of two heterostructure catalysts, A-TiO$_2$/CdSe and C-TiO$_2$/CdSe, were investigated using density functional theory (DFT) calculations. First, to examine the charge transfer from CdSe to TiO$_2$ of the two heterostructures, we inspected the charge difference based on the Bader charge analysis [40] in Fig. 8a. Unlike the charge difference in C-TiO$_2$/CdSe, the electron accumulation of Ti in A-TiO$_2$/CdSe appears on the TiO$_2$ surface and the interface between TiO$_2$ and CdSe. Therefore, the accumulated electrons in the surface Ti of A-TiO$_2$/CdSe can assist electron transfer to CO$_2$ for its photoreduction. The reduced work function of A-TiO$_2$/CdSe (4.41 eV vs. 5.07 eV of C-TiO$_2$/CdSe, Fig. S41) also supports that A-TiO$_2$/CdSe will have smaller electron migration energy from bulk to surface than C-TiO$_2$/CdSe [62].

The spin density in Fig. 8b shows that the surface photoexcited electron in Ti^{3+} of A-TiO$_2$/CdSe is more readily transferred to CO$_2$ molecule than C-TiO$_2$/CdSe. Therefore, CO$_2$ can be readily adsorbed on the surface and distort its geometry into a bent shape, which is evidence of lowered LUMO for further facile reduction processes [22]. The charge density difference in Fig. S42 illustrates the electron transfer from Ti to CO$_2$ in A-TiO$_2$/CdSe.

On the other hand, CO$_2$ in C-TiO$_2$/CdSe is hardly adsorbed on the surface since no Ti^{3+} site is available on the surface. Therefore, neither spin density (Fig. 8b) nor charge density difference (Fig. S42) show effective charge transfer to CO$_2$, resulting in a significant difference in the quantitative amount of charge transferred to C of CO$_2$ (-0.25e in A-TiO$_2$/CdSe vs −0.03e in C-TiO$_2$/CdSe). As a result, CO$_2$ is more strongly adsorbed on A-TiO$_2$/CdSe (-0.61 eV) than C-TiO$_2$/CdSe (-0.17 eV) for preferable CO$_2$ activation and reduction.

The generation of Ti^{3+} sites in A-TiO$_2$/CdSe is proven in the core level shifts of Ti 2p states in the two heterostructures in Fig. S43. In A-TiO$_2$/CdSe, the Ti^{3+} shoulder peak appeared on a lower binding energy

than Ti^{4+}, whereas there is only a Ti^{4+} peak in C-TiO$_2$/CdSe. The difference in Ti's density of up-spin and down-spin states in Fig. 8c elucidates that the spin symmetry in A-TiO$_2$/CdSe is more asymmetric than C-TiO$_2$/CdSe owing to less symmetric amorphous structure. Therefore, as illustrated in Fig. 8d, electron-hole separation of lower band (LB) in Ti 3d states is promoted in A-TiO$_2$/CdSe, where electrons in spin-up LB (SU-LB) state can be stably localised to Ti^{3+} and used for CO$_2$ reduction. Facile electron-hole separation in A-TiO$_2$/CdSe is attributed to Ti atoms' diverse and decreased coordination state, as shown in Fig. S44. Ti atoms in C-TiO$_2$/CdSe mostly have octahedral symmetry, which is saturated and inert with electron transfer from one to another. On the other hand, A-TiO$_2$ with asymmetric structure has a network structure of coordinately unsaturated and relatively saturated Ti-O$_n$ polyhedra that can efficiently transfer and localise electrons and thus can separate electrons far away from the interface of TiO$_2$/CdSe and expose them to surface with active sites. As reported previously [23], the electron localisation to the lower conduction band (LB) also activates oxygen vacancy formation that can act as a binding pocket for CO$_2$, and it is proven by the favourable vacancy formation energy in A-TiO$_2$/CdSe than C-TiO$_2$/CdSe in Fig. S45.

Based on the overall results, two different pathways for CO$_2$ photoreduction are proposed for two different heterostructures: formyl and formaldehyde for C−TiO$_2$/CdSe and A−TiO$_2$/CdSe, respectively. Regeneration in C−TiO$_2$/CdSe is challenging due to the limited active sites, which led to the deactivation of the photocatalyst. When Cd-deficient states become oxides, charge transfer at the heterostructure interface is hindered, resulting in the reaction pathway shown in Fig. 9a. In contrast to the intriguing properties of the A−TiO$_2$/CdSe, the photocatalyst was initially white but turned blackish-violet during the reaction. This confirms the formation of Ti^{3+} during the reaction, which enhances the interaction with the CO$_2$ molecules [63,64]. Fig. 9b shows Ti^{3+} returns to its original state (Ti^{4+}) after CO$_2$ photoreduction is complete. After a continuous electron supply by the CdSe, Ti^{4+} regenerates Ti^{3+}, and the process continues. We recorded a video during the reaction period to demonstrate this cycle (and the video is included in SI: **MP4**). As shown in Fig. 9b, the colour changes during the reaction as a function of time. After the reaction, the reactor was opened to allow the photocatalyst to interact with the surrounding atmosphere. As a result, the photocatalyst returned from its black-violet state to its initial
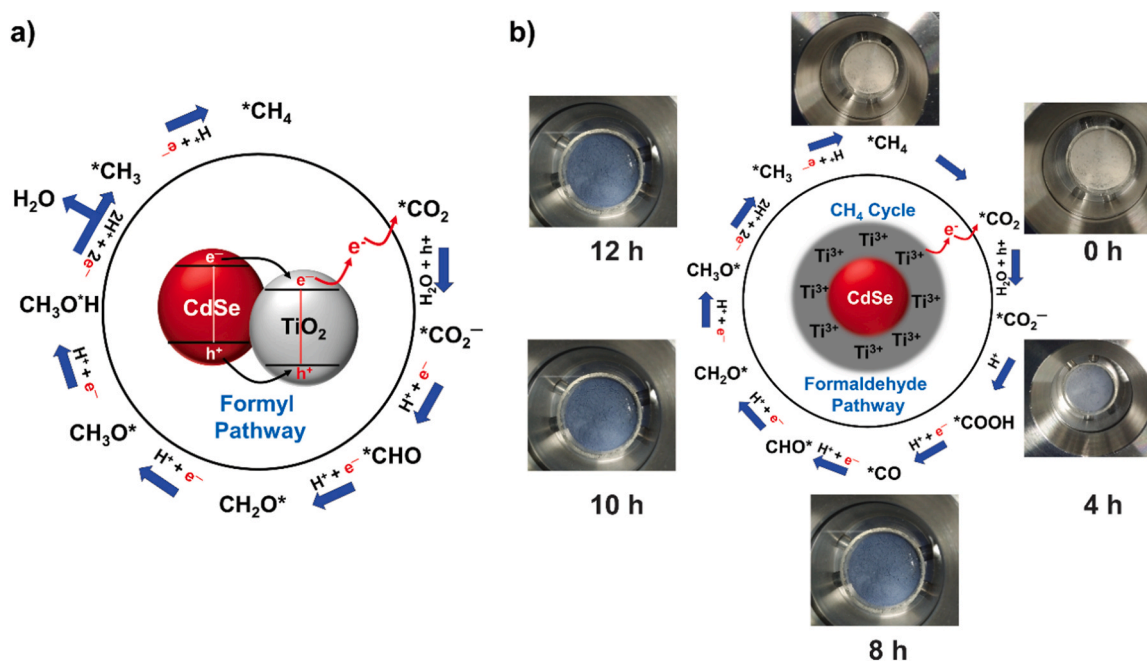

Fig. 9. Proposed mechanism for CO$_2$ photoreduction to CH$_4$ formation: a) C−TiO$_2$/CdSe and b) A−TiO$_2$/CdSe.

state. This shows that Ti^{3+} interacts with CO_2 molecules during the chemical reaction. Fig. 9b shows that the A—TiO_2/CdSe heterostructure revealed the CH_4 cycle with the formaldehyde pathway. The Ti^{3+}-Ti^{4+} cycle observed in the A-TiO_2/CdSe heterostructure plays a crucial role in enhancing the dynamics of the photogenerated charge carriers and influences the reaction selectivity during the photocatalytic reduction of CO_2. The formation of Ti^{3+} states, confirmed by core level shifts in the Ti 2p states, facilitates efficient electron-hole separation in the lower band of Ti 3d states. This asymmetry in the spin symmetry, due to the diverse and reduced coordination state of the Ti atoms in the A-TiO_2 structure, promotes the stable localisation of electrons in the spin-up SU-LB. The Ti^{3+}-Ti^{4+} cycle shows a dynamic interplay between the reduction of Ti^{4+} to Ti^{3+} during the reaction, favoured by the continuous electron supply of CdSe, and the subsequent regeneration of Ti^{4+} after the completion of CO_2 photoreduction. The efficient Ti^{3+}-Ti^{4+} cycle thus improves carrier dynamics by maintaining an active pool of electrons for CO_2 activation. This ultimately influences the reaction selectivity towards formaldehyde production in the photocatalytic process [65].

Supplementary material related to this article can be found online at doi:10.1016/j.apcatb.2024.124006.

6. Conclusion

In this study, two distinct heterostructures were meticulously engineered, namely C—TiO_2 and A—TiO_2, both incorporating CdSe, for photocatalytic CO_2 reduction. These heterostructures were strategically designed to optimise light absorption and facilitate efficient charge transport at their interfaces. The C—TiO_2/CdSe exhibited a remarkable dominance in light absorption, making them highly efficient in CO_2 photoreduction. In contrast, the A—TiO_2/CdSe demonstrated enhanced activity due to Ti^{3+} active sites. One of the notable findings of our work is the regeneration of Ti^{3+} active sites after CO_2 photoreduction, which revealed the existence of a CH_4 cycle. Ti^{3+} played a pivotal role in boosting CO_2 photoreduction activity, resulting in a threefold increase in performance compared to C—TiO_2/CdSe. However, the A—TiO_2/CdSe did not achieve the expected CO_2 photoreduction activity under multi-sun conditions, possibly due to the trapped energy state generating heat that hindered their performance. During the 7-sun analysis, the A—TiO_2/CdSe experienced a maximum thermal effect of 70°C, whereas the C—TiO_2/CdSe encountered a maximum thermal effect of 58°C. Additional analysis revealed the conversion of Ti^{3+} to Ti^{4+} before and after the reaction, further confirming their role in the photocatalytic process. A DFT study provided insights into the strong electron transfer between A—TiO_2 and CdSe, promoting the formation of active Ti^{3+} sites on the surface to reduce CO_2 molecules. Furthermore, DRIFTS analysis illuminated different intermediate steps of CO_2 photoreduction, highlighting the formaldehyde pathway on the A—TiO_2 surface and the formyl pathway on the C—TiO_2 surface. These observations underscored the distinct interactions between crystalline and amorphous photocatalytic surfaces and CO_2 molecules. Finally, the study demonstrated the stability of C—TiO_2/CdSe for 18 h and the potential recyclability of A—TiO_2/CdSe, indicating their promise as precious metal-free surface-optimised photocatalysts. This research opens new avenues for developing smart photocatalysts tailored for specific fine chemical synthesis applications.

CRediT authorship contribution statement

Niket Powar: Writing – review & editing, Writing – original draft, Methodology, Formal analysis, Data curation, Conceptualization. **Sanghoon Kim:** Writing – review & editing, Writing – original draft, Software, Formal analysis. **Junho Lee:** Formal analysis. **Eunhee Gong:** Formal analysis. **Chaitanya B. Hiragond:** Validation. **Dongyun Kim:** Validation. **Tierui Zhang:** Validation. **Minho Kim:** Writing – review & editing, Writing – original draft, Software, Formal analysis, Data curation. **Su-Il In:** Writing – review & editing, Writing – original draft, Supervision, Project administration, Methodology, Investigation, Funding acquisition, Conceptualization.

Declaration of Competing Interest

The authors declare that they have no known competing financial interests or personal relationships that could have appeared to influence the work reported in this paper.

Data availability

Data will be made available on request.

Appendix A. Supporting information

Supplementary data associated with this article can be found in the online version at doi:10.1016/j.apcatb.2024.124006.

References

[1] J. Su, L. Vayssieres, A place in the sun for artificial photosynthesis? ACS Energy Lett. 1 (2016) 121–135.
[2] E. Gong, S. Ali, C.B. Hiragond, H.S. Kim, N.S. Powar, D. Kim, H. Kim, S.-I. In, Solar fuels: research and development strategies to accelerate photocatalytic CO_2 conversion into hydrocarbon fuels, Energy Environ. Sci. 15 (2022) 880–937.
[3] S. Ali, J. Lee, H. Kim, Y. Hwang, A. Razzaq, J.-W. Jung, C.-H. Cho, S.-I. In, Sustained, photocatalytic CO_2 reduction to CH_4 in a continuous flow reactor by earth-abundant materials: Reduced titania-Cu_2O Z-scheme heterostructures, Appl. Catal. B 279 (2020) 119344.
[4] C.B. Hiragond, J. Lee, H. Kim, J.-W. Jung, C.-H. Cho, S.-I. In, A novel N-doped graphene oxide enfolded reduced titania for highly stable and selective gas-phase photocatalytic CO_2 reduction into CH_4: An in-depth study on the interfacial charge transfer mechanism, Chem. Eng. J. 416 (2021) 127978.
[5] N.S. Powar, C.B. Hiragond, D. Bae, S.-I. In, Two-dimensional metal carbides for electro-and photocatalytic CO_2 reduction, J. CO_2 Util. 55 (2022) 101814.
[6] F. Xu, K. Meng, B. Cheng, S. Wang, J. Xu, J. Yu, Unique S-scheme heterojunctions in self-assembled TiO_2/$CsPbBr_3$ hybrids for CO_2 photoreduction, Nat. Commun. 11 (2020) 4613.
[7] X. Han, B. Lu, X. Huang, C. Liu, S. Chen, J. Chen, Z. Zeng, S. Deng, J. Wang, Novel p-and n-type S-scheme heterojunction photocatalyst for boosted CO_2 photoreduction activity, Appl. Catal. B 316 (2022) 121587.
[8] J. Bian, Z. Zhang, J. Feng, M. Thangamuthu, F. Yang, L. Sun, Z. Li, Y. Qu, D. Tang, Z. Lin, Energy Platform for Directed Charge Transfer in the Cascade Z-Scheme Heterojunction: CO_2 Photoreduction without a Cocatalyst, Angew. Chem. 133 (2021) 21074–21082.
[9] S. Sorcar, Y. Hwang, C.A. Grimes, S.-I. In, Highly enhanced and stable activity of defect-induced titania nanoparticles for solar light-driven CO_2 reduction into CH_4, Mater. Today 20 (2017) 507–515.
[10] C.J. Gagliardi, B.C. Westlake, C.A. Kent, J.J. Paul, J.M. Papanikolas, T.J. Meyer, Integrating proton coupled electron transfer (PCET) and excited states, Coord. Chem. Rev. 254 (2010) 2459–2471.
[11] H. Khan, R.C. Pawar, H. Charles, C.S. Lee, Cu-doped TiO_2 nanofibers coated with 1T $MoSe_2$ nanosheets providing a conductive pathway for the electron separation in CO_2 photoreduction, Appl. Surf. Sci. 636 (2023) 157832.
[12] H. Charles, R.C. Pawar, H. Khan, P.J. Chengula, C.S. Lee, Double-sided growth of $MoSe_2$ nanosheets onto hollow zinc stannate (ZnO, $ZnSnO_3$, and SnO_2) nanofibers (h-ZTO) for efficient CO_2 photoreduction, J. Environ. Chem. Eng. 11 (2023) 109917.
[13] H. Shi, S. Long, S. Hu, J. Hou, W. Ni, C. Song, K. Li, G.G. Gurzadyan, X. Guo, Interfacial charge transfer in 0D/2D defect-rich heterostructures for efficient solar-driven CO_2 reduction, Appl. Catal. B 245 (2019) 760–769.
[14] X. Jin, J. Cao, H. Wang, C. Lv, H. Xie, F. Su, X. Li, R. Sun, S. Shi, M. Dang, Realising improved CO_2 photoreduction in Z-scheme $Bi_4O_5Br_2$/AgBr heterostructure, Appl. Surf. Sci. 598 (2022) 153758.
[15] J. Wang, Y. Yu, J. Cui, X. Li, Y. Zhang, C. Wang, X. Yu, J. Ye, Defective g-C_3N_4/ covalent organic framework van der Waals heterojunction toward highly efficient S-scheme CO_2 photoreduction, Appl. Catal. B 301 (2022) 120814.

[16] A. Hezam, K. Alkanad, M.A. Bajiri, J. Strunk, K. Takahashi, Q.A. Drmosh, N. Al-Zaqri, L.N. Krishnappagowda, 2D/1D MoS$_2$/TiO$_2$ heterostructure photocatalyst with a switchable CO$_2$ reduction product, Small Methods 7 (2023) 2201103.

[17] J. Tu, H. Wu, Q. Qian, S. Han, S. Chu, S. Jia, R. Feng, J. Zhai, M. He, B. Han, Low temperature methanation of CO$_2$ over an amorphous cobalt-based catalyst, Chem. Sci. 12 (2021) 3937–3943.

[18] C. Chen, X. Yan, Y. Wu, X. Zhang, S. Liu, F. Zhang, X. Sun, Q. Zhu, L. Zheng, J. Zhang, Oxidation of metallic Cu by supercritical CO$_2$ and control synthesis of amorphous nano-metal catalysts for CO$_2$ electroreduction, Nat. Commun. 14 (2023) 1092.

[19] Y. Wei, F. You, D. Zhao, J. Wan, L. Gu, D. Wang, Heterogeneous Hollow Multi-Shelled Structures with Amorphous-Crystalline Outer-Shells for Sequential Photoreduction of CO$_2$, Angew. Chem. Int. Ed. 61 (2022) e202212049.

[20] C. Wang, R.L. Thompson, J. Baltrus, C. Matranga, Visible light photoreduction of CO$_2$ using CdSe/Pt/TiO$_2$ heterostructured catalysts, J. Phys. Chem. Lett. 1 (2010) 48–53.

[21] J. Fu, K. Jiang, X. Qiu, J. Yu, M. Liu, Product selectivity of photocatalytic CO$_2$ reduction reactions, Mater. Today 32 (2020) 222–243.

[22] A. Álvarez, M. Borges, J.J. Corral-Pérez, J.G. Olcina, L. Hu, D. Cornu, R. Huang, D. Stoian, A. Urakawa, CO$_2$ activation over catalytic surfaces, ChemPhysChem 18 (2017) 3135–3141.

[23] B.-H. Lee, E. Gong, M. Kim, S. Park, H.R. Kim, J. Lee, E. Jung, C.W. Lee, J. Bok, Y. Jung, Electronic interaction between transition metal single-atoms and anatase TiO$_2$ boosts CO$_2$ photoreduction with H$_2$O, Energy Environ. Sci. 15 (2022) 601–609.

[24] N.S. Powar, M. Jang, M.G. Kim, C.B. Hiragond, J. Lee, E. Gong, H. Kim, D. Kim, J.-W. Jung, C.-H. Cho, Dynamic Ti^{3+} and In^{3+} dual active sites on In$_2$TiO$_5$ to enhance visible-light-driven gas-phase photocatalytic CO$_2$ reduction, Chem. Eng. J. (2023) 147966.

[25] R. Nawaz, C.F. Kait, H.Y. Chia, M.H. Isa, L.W. Huei, N.T. Sahrin, N. Khan, Manipulation of the Ti^{3+}/Ti^{4+} ratio in colored titanium dioxide and its role in photocatalytic degradation of environmental pollutants, Surf. Interfaces 32 (2022) 102146.

[26] Y. Ji, W. Guo, H. Chen, L. Zhang, S. Chen, M. Hua, Y. Long, Z. Chen, Surface Ti^{3+}/Ti^{4+} redox shuttle enhancing photocatalytic H2 production in ultrathin TiO$_2$ nanosheets/CdSe quantum dots, J. Phys. Chem. C. 119 (2015) 27053–27059.

[27] Z. Li, C. Mao, Q. Pei, P.N. Duchesne, T. He, M. Xia, J. Wang, L. Wang, R. Song, F. M. Ali, Engineered disorder in CO$_2$ photocatalysis, Nat. Commun. 13 (2022) 7205.

[28] N.S. Powar, D. Kim, S. In, Toward a Comprehensive Understanding of Amorphous Photocatalysts: Fundamental Hypotheses and Applications in CO$_2$ Photoreduction, Chemistry, A Eur. J. (2023) e202203810.

[29] Y. Wei, J. Wan, N. Yang, Y. Yang, Y. Ma, S. Wang, J. Wang, R. Yu, L. Gu, L. Wang, Efficient sequential harvesting of solar light by heterogeneous hollow shells with hierarchical pores, Natl. Sci. Rev. 7 (2020) 1638–1646.

[30] H. Wang, D. Wu, C. Yang, H. Lu, Z. Gao, F. Xu, K. Jiang, Multi-functional amorphous TiO$_2$ layer on ZIF-67 for enhanced CO$_2$ photoreduction performances under visible light, J. CO2 Util. 34 (2019) 411–421.

[31] D. Du, W. Shi, L. Wang, J. Zhang, Yolk-shell structured Fe$_3$O$_4$@ void@ TiO$_2$ as a photo-Fenton-like catalyst for the extremely efficient elimination of tetracycline, Appl. Catal. B 200 (2017) 484–492.

[32] F. Fresno, P. Reñones, E. Alfonso, C. Guillén, J.F. Trigo, J. Herrero, L. Collado, V. A. de la Peña O'Shea, Influence of surface density on the CO$_2$ photoreduction activity of a DC magnetron sputtered TiO2 catalyst, Appl. Catal. B 224 (2018) 912–918.

[33] L. Xu, Y. Ren, Y. Fu, M. Liu, F. Zhu, M. Cheng, J. Zhou, W. Chen, K. Wang, N. Wang, Strong photo-thermal coupling effect boosts CO$_2$ reduction into CH$_4$ in a concentrated solar reactor, Chem. Eng. J. (2023) 143831.

[34] G. Kresse, Google Scholar Crossref, ISI G. Kresse and J. Hafner, Phys. Rev. B Https://Doi. Org/10.1103/PhysRevB 49 (1994) 14251.

[35] G. Kresse, J. Furthmüller, Efficient iterative schemes for ab initio total-energy calculations using a plane-wave basis set, Phys. Rev. B 54 (1996) 11169.

[36] G. Kresse, J. Furthmüller, Efficiency of ab-initio total energy calculations for metals and semiconductors using a plane-wave basis set, Comput. Mater. Sci. 6 (1996) 15–50.

[37] J.P. Perdew, K. Burke, M. Ernzerhof, Generalised gradient approximation made simple, Phys. Rev. Lett. 77 (1996) 3865.

[38] S. Grimme, S. Ehrlich, L. Goerigk, Effect of the damping function in dispersion corrected density functional theory, J. Comput. Chem. 32 (2011) 1456–1465.

[39] G. Kresse, D. Joubert, From ultrasoft pseudopotentials to the projector augmented-wave method, Phys. Rev. B 59 (1999) 1758.

[40] G. Henkelman, A. Arnaldsson, H. Jónsson, A fast and robust algorithm for Bader decomposition of charge density, Comput. Mater. Sci. 36 (2006) 354–360.

[41] K. Momma, F. Izumi, VESTA 3 for three-dimensional visualisation of crystal, volumetric and morphology data, J. Appl. Crystallogr 44 (2011) 1272–1276.

[42] H. Charles, P.J. Chengula, R.C. Pawar, H. Khan, S. Kim, C.S. Lee, Synergistic effect of surface modification and effective interfacial charge transfer over faceted g-C$_3$N$_4$/ZnSe heterojunction to enhance CO$_2$ photoreduction activity, J. Water Process Eng. 56 (2023) 104307.

[43] H.G. Yang, C.H. Sun, S.Z. Qiao, J. Zou, G. Liu, S.C. Smith, H.M. Cheng, G.Q. Lu, Anatase TiO$_2$ single crystals with a large percentage of reactive facets, Nature 453 (2008) 638–641.

[44] D. Nath, F. Singh, R. Das, X-ray diffraction analysis by Williamson-Hall, Halder-Wagner and size-strain plot methods of CdSe nanoparticles-a comparative study, Mater. Chem. Phys. 239 (2020) 122021.

[45] Z. Gao, H. Yang, J. Mao, L. Kang, R. Zhang, S. Chai, J. Wu, W. Li, Araneose Ti^{3+} self-doping TiO$_2$/SiO$_2$ nanowires membrane for removal of aqueous MB under visible light irradiation, Environ. Sci. Pollut. Res. 27 (2020) 9748–9759.

[46] M.-Y. Huang, X.-B. Li, Y.-J. Gao, J. Li, H.-L. Wu, L.-P. Zhang, C.-H. Tung, L.-Z. Wu, Surface stoichiometry manipulation enhances solar hydrogen evolution of CdSe quantum dots, J. Mater. Chem. A Mater. 6 (2018) 6015–6021.

[47] Y. Cao, L. Guo, M. Dan, D.E. Doronkin, C. Han, Z. Rao, Y. Liu, J. Meng, Z. Huang, K. Zheng, Modulating electron density of vacancy site by single Au atom for effective CO$_2$ photoreduction, Nat. Commun. 12 (2021) 1675.

[48] J. Dhakshinamoorthy, A.K. Prasad, S. Dhara, B. Pullithadathil, Anomalous effects of lattice strain and Ti^{3+} interstitials on room-temperature magnetic ordering in defect-engineered nano-TiO$_2$, J. Phys. Chem. C. 122 (2018) 27782–27794.

[49] N. Cao, Z. Chen, K. Zang, J. Xu, J. Zhong, J. Luo, X. Xu, G. Zheng, Doping strain induced bi-Ti^{3+} pairs for efficient N$_2$ activation and electrocatalytic fixation, Nat. Commun. 10 (2019) 2877.

[50] O. Frank, M. Zukalova, B. Laskova, J. Kürti, J. Koltai, L. Kavan, Raman spectra of Titanium Dioxide (Anatase, Rutile) with Identified Oxygen Isotopes, (n.d.).

[51] Y. Zhang, X. Yang, X. Yang, H. Duan, H. Qi, Y. Su, B. Liang, H. Tao, B. Liu, D. Chen, Tuning reactivity of Fischer–Tropsch synthesis by regulating TiO$_x$ overlayer over Ru/TiO$_2$ nanocatalysts, Nat. Commun. 11 (2020) 3185.

[52] H. Zhang, S. Zuo, M. Qiu, S. Wang, Y. Zhang, J. Zhang, X.W. Lou, Direct probing of atomically dispersed Ru species over multi-edged TiO$_2$ for highly efficient photocatalytic hydrogen evolution, Sci. Adv. 6 (2020) eabb9823.

[53] D. Cabaret, Y. Joly, H. Renevier, Pre-edge structure analysis of Ti K-edge polarised X-ray absorption spectra in TiO$_2$ by full-potential XANES calculations, J. Synchrotron Radiat. 6 (1999) 258–260.

[54] M. Ahmadi, J. Timoshenko, F. Behafarid, B. Roldan Cuenya, Tuning the structure of Pt nanoparticles through support interactions: an in situ polarised X-ray absorption study coupled with atomistic simulations, J. Phys. Chem. C. 123 (2019) 10666–10676.

[55] J. Zheng, J. Lyu, R. Wang, C. Xie, H. Zhou, S.P. Jiang, S. Wang, Crystalline TiO$_2$ protective layer with graded oxygen defects for efficient and stable silicon-based photocathode, Nat. Commun. 9 (2018) 3572.

[56] C. Wang, X. Kang, J. Liu, D. Wang, N. Wang, J. Chen, J. Wang, C. Tian, H. Fu, Ultrathin black TiO$_2$ nanosheet-assembled microspheres with high stability for efficient solar-driven photocatalytic hydrogen evolution, Inorg. Chem. Front 10 (2023) 1153–1163.

[57] U. Diebold, The surface science of titanium dioxide, Surf. Sci. Rep. 48 (2003) 53–229.

[58] J.-S. Lee, M.V. Kovalenko, J. Huang, D.S. Chung, D.V. Talapin, Band-like transport, high electron mobility and high photoconductivity in all-inorganic nanocrystal arrays, Nat. Nanotechnol. 6 (2011) 348–352.

[59] F. Zhang, Y.-H. Li, M.-Y. Qi, Y.M.A. Yamada, M. Anpo, Z.-R. Tang, Y.-J. Xu, Photothermal catalytic CO$_2$ reduction over nanomaterials, Chem. Catal. (2021).

[60] S. Bhattacharjee, U.V. Waghmare, S.-C. Lee, An improved d-band model of the catalytic activity of magnetic transition metal surfaces, Sci. Rep. 6 (1) (2016) 10.

[61] S.J. Yun, G. Lee, J.S. Kim, S.K. Shin, Y.-G. Yoon, Electronic structure and optical absorption spectra of CdSe covered with ZnSe and ZnS epilayers, Solid State Commun. 137 (2006) 332–337.

[62] J. Xiong, A. Yang, Q. Sun, H. Gao, H. Zhang, Y. Mao, Z. Liang, Insights into CO$_2$ activation and charge transfer in photocatalytic reduction of CO$_2$ on pure and metal single atom modified TiO$_2$ surfaces, Mol. Catal. 547 (2023) 113370.

[63] L. Lin, Y. Ma, J. Wu, F. Pang, J. Ge, S. Sui, Y. Yao, R. Qi, Y. Cheng, C. Duan, Origin of photocatalytic activity in Ti^{4+}/Ti^{3+} core–shell titanium oxide nanocrystals, J. Phys. Chem. C. 123 (2019) 20949–20959.

[64] X. Xin, T. Xu, L. Wang, C. Wang, Ti^{3+}-self doped brookite TiO$_2$ single-crystalline nanosheets with high solar absorption and excellent photocatalytic CO$_2$ reduction, Sci. Rep. 6 (2016) 1–8.

[65] G. Yin, X. Huang, T. Chen, W. Zhao, Q. Bi, J. Xu, Y. Han, F. Huang, Hydrogenated blue titania for efficient solar to chemical conversions: preparation, characterisation, and reaction mechanism of CO$_2$ reduction, ACS Catal. 8 (2018) 1009–1017.